EXPERIMENTAL AND NUMERICAL INVESTIGATION OF THE FRACTURE TOUGHNESS OF SHAPE MEMORY ALLOYS

by
Jasdeep Makkar

A dissertation submitted to the Department of Materials Science and Engineering,
Cullen College of Engineering
in partial fulfillment of the requirements for the degree of

Doctor of Philosophy
in Materials Science and Engineering

Chair of Committee: Dr. Theocharis Baxevanis

Committee Member: Dr. Yashashree Kulkarni

Committee Member: Dr. Gangbing Song

Committee Member: Dr. Dong Liu

Committee Member: Dr. Dimitrios Kalliontzis

University of Houston
December 2021

ACKNOWLEDGMENTS

The real gift of gratitude is that the more grateful you are, the more present you become. I would really like to thank everyone who played their role in helping me reach where I am today. Credit to those who motivated and inspired me sail through tough tides and helped me to complete my doctoral studies.

A teacher is a compass that activates the magnets of curiosity, knowledge, and wisdom in the pupils. I would like to appreciate all the effort and time invested by Dr. Theocharis Baxevanis, my Ph.D. advisor, without him, this won't be possible. His guidance and shared knowledge have piqued my interest in research and certainly changed my perspective. His 'you can do' approach have encouraged me to accomplish tasks deemed impossible and helped me attain recognition in the scientific community. Better than a thousand days of diligent study is one day with a great teacher. I would like to acknowledge my committee members, Dr. Yashashree Kulkarni, Dr. Gangbing Song, Dr. Dong Liu, Dr. Dimitrios kalliotzis, and Dr. Theocharis Baxevanis for reviewing my dissertation and giving valuable suggestions and comments.

This research work was supported by the US Air Force Office of Scientific Research under Grant No. FA9550-18-1-0276, the National Science Foundation under Grants no. CMMI-1917441 and CMMI-1917367, and by NASA-ULI under Grant No. NNX17AJ96A.

At the end of the day, the most overwhelming key to a person's success is the positive involvement of parents. I would like to dedicate my dissertation to my parents Mr. Jagjeet Makkar and Mrs. Avneet Makkar, without their unconditional support and love this won't be possible. Special thanks to my brother Namandeep Makkar who always believed in me and my grandmother Mrs. Jagdish Kaur Makkar, who made me a noble human and will always be in my thoughts.

Jasdeep Makkar

December 02, 2021

ABSTRACT

Shape Memory Alloys (SMAs) are intermetallics with unique properties emanating from a reversible diffussionless solid to solid phase transformation from a stable at high temperatures phase (austenite) to a stable at low temperatures phase (martensite). Attributed to their efficacy to generate large recoverable strains by undergoing thermomecanically-induced phase transformation, SMAs emerge as leading preference for various applications in aerospace, outer space, transportation, construction, and biomedical industry. To ensure ascendancy of the SMAs for such applications, understanding their failure behavior and standardization of fracture toughness measurements are imperative in the realm of fracture mechanics methods to provide structural integrity assessment, damage tolerance design, performance evaluation, quality assurance, among others. The fracture response of SMAs is rather complex due to (re)orientation of martensite variants, reversibility of phase transformation, transformation-induced plasticity, latent heat effects, and possible co-existence of cleavage fracture and ductile tearing. SMAs display stable crack growth, a fracture toughening response attributed to energy dissipation due to phase transformation occurring close to the crack tip, under nominally isothermal conditions, similarly to other dissipative material systems, as well as under "actuation" loading such as isobaric thermal variations. The aim of this dissertation is (i) to propose necessary modifications to the existing ASTM standards, which have been developed for conventional structural metals, for the experimental measurement of fracture toughness of SMAs; (ii) experimentally examine the effect of the reversibility of phase transformation on the transformation-induced fracture toughness enhancement; (iii) propose a path-independent contour integral for describing the driving force for crack growth in SMAs under thermomechanical (actuation) loading paths, which collapses to the J-integral under nominally-isothermal conditions, and experimentaly measure the fracture toughness under isobaric conditions; and (iv) investigate void growth and

coalescence in precipitation-hardened SMAs by unit cell simulations and, by comparison to the available experimental data, draw conclusions on their importance on the fracture response of these materials.

TABLE OF CONTENTS

LIST OF TABLES

LIST OF FIGURES

1 Introduction

1.1 Introduction to Shape Memory Alloys (SMAs)

1.1.1 Existence and history of SMAs

The existence of every man-made structure requires three aspects to be addressed, the availability of materials, utilization of improved materials, and human vision to capitalize on the previous two aspects to convert one's vision into realistic designs. With the advancement of science and technology, traditional materials may not be suitable for future goals. Hence, there is an increasing demand for advanced, lighter, and stronger materials that can provide multi-functional properties. A specialized subgroup of materials that can be used for actuation purposes, impact absorption, and vibration damping applications are known as 'active materials' to which Shape Memory Alloys (SMAs) belong. SMAs' mechanical, thermal, magnetic, and electrical capabilities stand out in that category [68, 38, 97, 47, 124]. SMAs are being prioritized for most of the above mentioned applications because of their high actuation energy density and high actuation frequency as compared to other active materials, which can be observed in Figure 1.

Initially, in late 19^{th} century martensitic transformation was first observed in ferric steels, which was later used as the basis to work on concepts like thermoelastic martensitic transformation and reversible transformation of martensite for copper based alloys in mid 20^{th} century by [85]. Utilization of these processes in engineering applications was not implemented until the discovery of nickel titanium alloys in 1963 [26], where they were trying to investigate materials useful for heat shielding, and this discovery led to the basis of SMAs and its utilization in various engineering applications with nickel-titanium alloys(NiTi) most extensively researched at "Nitinol" [68]. Later, interplay between the atomic weight variations [68] and addition

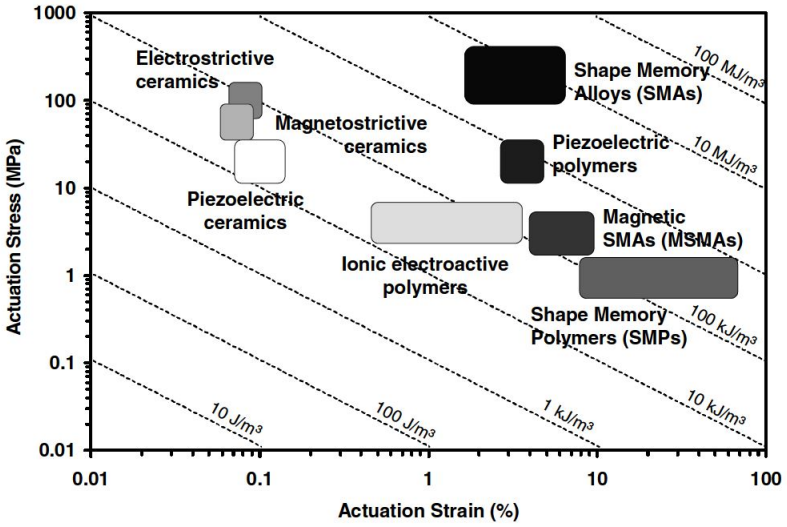

Figure 1: Actuation energy density plot showing different ranges of actuation stress, actuation strain, and the actuation energy densities of different active materials (After [88]).

of third element [163] helped change the transition temperatures, stress hysteresis length [170], fatigue life [118], and deformation behavior [115] of these materials that opened numerous possibilities for SMAs to be used commercially in various fields, which will be discussed in the next section.

1.1.2 Commercial use of SMAs

Owing to high actuation energy, high actuation frequency, and the ability of SMAs to provide an output through mechanical, thermal, electrical, or magnetic input, they are utilized in various industries such as aerospace [96], spacecrafts [169], medical [23] and transportation [8]. In this section, we will discuss a few of these engineered technologies, which will give an insight into the fact that possibilities through these smart materials are limitless.

Due to the capability of SMAs to achieve their full potential at variable scale lengths, they were used as variable geometry airfoil [155]. In this application, their

actuation property was utilized where the airfoil effectively changed its shape from symmetric to chambered. Taking into account their ability to absorb energy and use this energy for phase transformation, they helped in optimizing the size and shape of aircraft structural panels, where thermally-induced post-buckling deflection of a structure was decreased [156]. SMAs have also been used in space applications to address problems in zero atmosphere environment where it deals with actuation and release purposes. Fourteen percent of space missions experienced failure due to shock and vibration during spacecraft launch, these issues can be sorted using SMAs energy absorption capabilities [52].

The shape memory and pseudo-elastic properties discussed in the next section, coupled with the biofunctionality and biocompatibility of NiTi, make it a suitable candidate for medical applications [144, 100]. The amalgamation of these unique characteristics has led to the unraveling of various applications such as stents [37], filters, orthodontic wires [3], orthopedic replacements for fractured bones or injured ligaments as well as devices for minimally invasive surgery (MIS) [147, 144]. Porous SMAs represent a different material form that can be used as an artificial bone implant [90]. The hysteric characteristic of SMAs helps to create systems that effectively dissipate vibrations and shocks. These systems are used in armored vehicles [127]. In commercial vehicles, they use SMA springs as sensors to monitor the temperature and to actuate the valve at a specific temperature, thereby changing the direction of the oil flow, which helps the car's continuous transmission [123].

All these applications and many more are achieved by utilizing various thermomechanical properties of SMAs, which are discussed in detail in sections below. All these abilities open a box of opportunities where these materials can be employed.

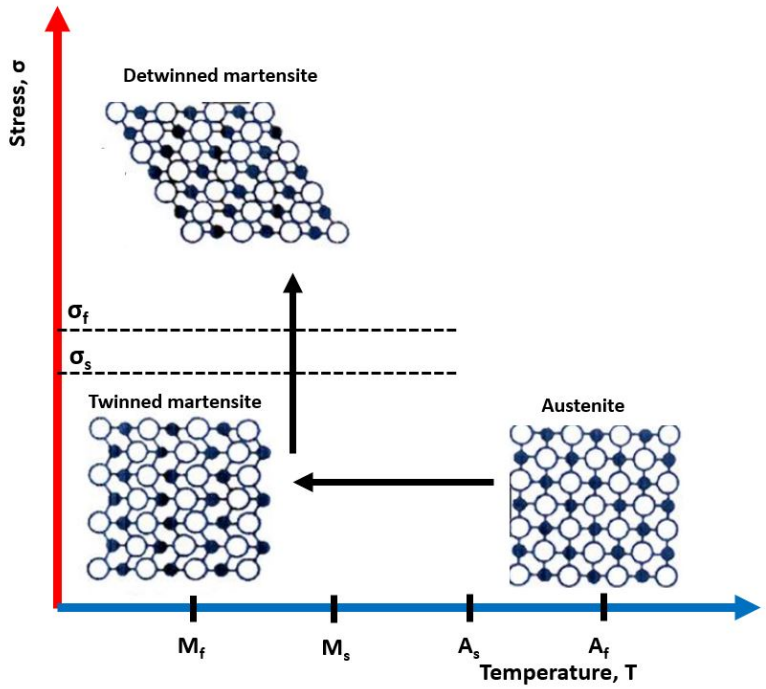

Figure 2: Stress-Temperature plot showing austenitic and martensitic crystallographic schematics.

1.2 Basic functionalities of SMAs

To make it easier to understand all major phenomenons of these complicated materials, it's important to have a basic knowledge of how we characterize them. They are categorized into two stable phases, each with a different crystal structure and therefore different properties. Austenite (A) is a high-temperature phase, also known as the parent phase, its crystal structure is usually cubic, and the other is a phase stable at low temperature called martensite (M) which has a different crystal structure depending on the composition, or the alloying element, which can make martensitic crystal structure tetragonal, orthorhombic, or monoclinic. Shift from a stable parent phase to low temperature phase can be induced through applied stress or temperature variation and such transformation is known as the martensitic transformation. One of the unique factors about these materials is that the transformation from one phase

to another is due to shear lattice distortion (moment of atoms from their original position) rather than the diffusion of atoms, an interesting aspect of such transformation is that it can be completely recovered when an external stimulus is relaxed as long as we are in linear elastic or non-linear elastic regime of these materials. This martensitic transformation can be further categorized into twinned martensite(M^t) and detwinned martensite(M^d) phases, whereas twinned martensite is a combination of "self accommodated" martensitic variants (martensitic crystals with different orientation direction) which means that the shape change will only be observed on microscopic scale *i.e.*, in the crystal structure. When a particular variant becomes dominant and grows at the expense of others, an observable shape change occurs at the microscopic scale as well as the macroscopic scale, that formation is termed as "detwinned martensite". Figure 2 shows schematic of these transformed phases on a stress-temperature plot.

1.2.1 Temperature-stress play of SMAs

In the above section, we have discussed different phases of SMAs but there is more to that, the interplay between these phases due to thermal, stress, or thermo-mechanical stimuli brings out various properties which can be used to innovate new technologies while utilizing limited resources, but it's important to understand those properties in-depth and more importantly, the terminology and working of SMAs phase diagram must be comprehended to acknowledge true work of art.

The phase diagram as shown in Figure 3 consists of temperature on the x-axis and stress on the y-axis, which shows the boundaries of the transformation regions in a stress-temperature space. The change of phase from austenite to martensite is known as forward transformation that can create several martensitic variants, possibly 24 for NiTi alloys. When transformation takes place from the martensitic phase back to

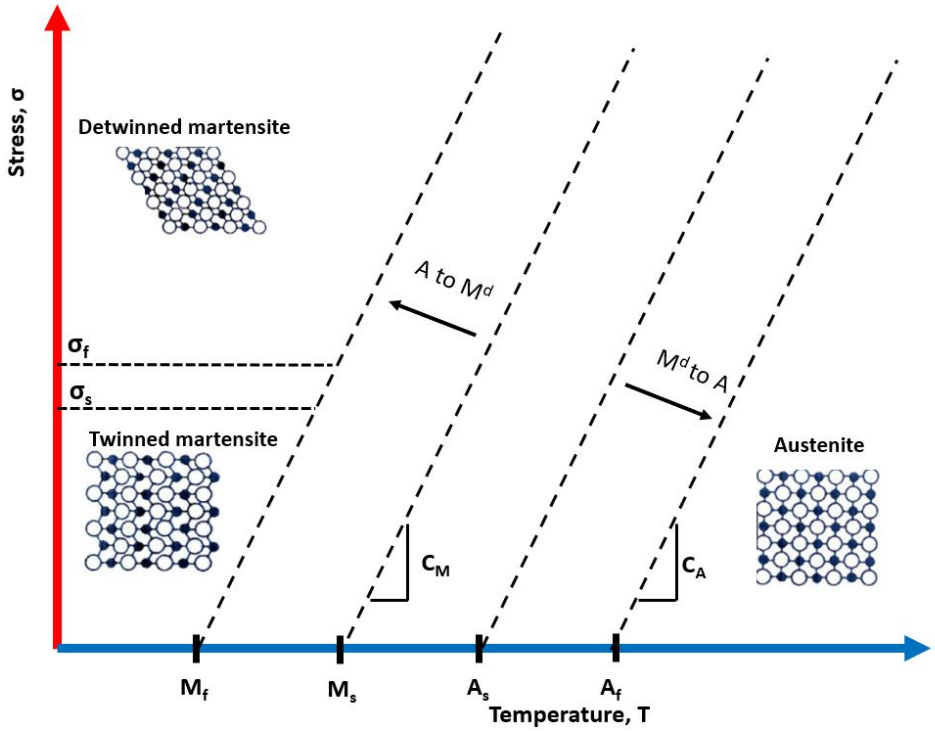

Figure 3: SMAs phase diagram in Stress and temperature space.

the high temperature phase, the crystal structure transforms back to cubic structure, and this transition is called reverse transformation.

Differential scanning calorimeter (DSC) testing is required to come with the zero stress transition temperatures such as A_f austenite finish temperature and A_s austenite start temperature that shows the initiation and completion of transformation from martensite to austenite. M_f martensite finish temperature and M_s martensite start temperature, respectively show initiation and completion of transformation from austenite to martensite at zero stress levels. But these temperatures are not sufficient to characterize the phase diagram completely and therefore slopes to the transformation surfaces must be known which helps us to know how much stress will be required at a certain temperature to initiate or complete the phase transformation or how much temperature variation will be required at a particular stress level to initiate or

finish forward or reverse phase transformation. C_M and C_A are know as stress influence coefficients or general slopes, and they play a vital role in completing the picture when understanding the phase diagrams of these materials. Transformation is also possible from twinned martensite to detwinned martensite and therefore the start and finish stress levels σ_s and σ_f for detwinned martensite must be known, which are evaluated through different experimental investigations. All these parameters vary with materials used to form an alloy, composition of metals, presence/absence and size of precipitates, oxides, and carbides, training of material and method adopted to create such alloys. Phase diagrams also vary if we add a new metal to increase/decrease the brittleness of those alloys.

This summarizes the basic knowledge of the phase diagram of SMAs. These characteristics help SMAs to attain certain properties, which are unique when compared to other intermetallic alloys and useful in various applications. Shape Memory Effect(SME) and pseudoelasticity are the most prominent and widely utilized properties of SMAs, which we will discuss in coming sections.

1.2.2 Shape memory effect

The basics of the shape memory effect can be understood completely by the stress-strain-temperature schematic in Figure 4 which is discussed below. SME simply deals with thermomechanical capabilities of these materials that show how we can go from austenite phase to detwinned martensite by applying sufficient amount of bias load while cooling the material, which provides large transformation strains. This type of complicated loading will not permanently deform the material as long as we are below plastic yielding stress values. It also shows how we can directly go from detwinned martensite phase to austenite by simply heating the specimen above austenitic finish temperature while that bias load is still there. This interplay between phases helps

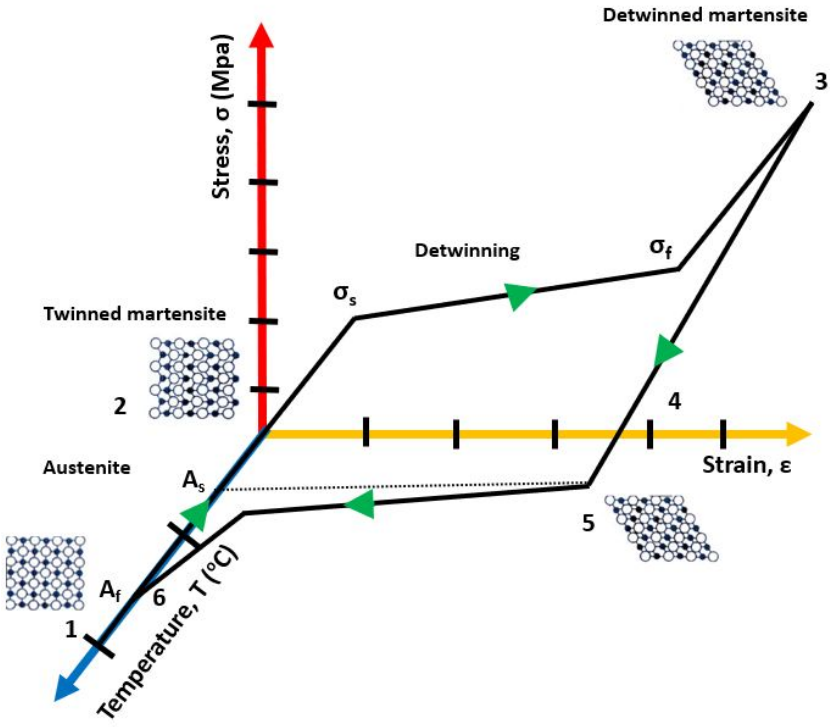

Figure 4: Schematic for shape memory effect using stress-strain-temperature space.

us to use different crystal structural characteristics of SMAs.

In order to explain the above phenomena in detail, we can show how a uniaxial loading response looks like in the stress-strain-temperature space. Initially, we are in the austenitic phase/parent phase of the material *i.e.*, above austenitic finish temperature, which is shown as point 1 in the Figure 4. If we start stress-free cooling below forward transformation temperature, the material will rearrange its crystal structure from cubic to twinned martensite's crystal structure where no macroscopic shape change is observed, but the mechanical properties of the system have completely changed at point 2. If we start applying load to the material in the twinned martensitic phase, it will start transforming to detwinned martensite as soon as stress levels hit (σ_s). From this point, reorientation process kicks in and a favorable martensitic variant will grow at the expense of others, usually this variant is in the direction of the

load applied. This eventuality also indicates the initiation of large recoverable transformation strains (ε_t), which is completed when stress levels reach (σ_f), that marks the complete formation of detwinned martensite, further, loading will elastically deform the material with material properties adhering to detwinned martensite crystal structure that can be seen at point 3. The magical part of SME can be observed from 3 to 4, where we elastically unload the material, but the detwinned martensitic state is retained so are the transformation strains. On heating in the absence of load will initiate the reverse transformation, as the temperature reaches austenitic start, at 5, the strains will start disappearing and this process of recovering the strains is completed at a temperature above austenitic finish at point 6, above which only the parent austenitic phase exists. If the stress applied were below permanent plastic yielding when the material was in detwinned martensite state, all strains will be recovered. The ability of SME to recover large strains during the reverse phase transformation from detwinned martensite phase to austenite using temperature variations is widely used for actuation purposes.

1.2.3 Pseudoelasticity

Pseudoelasticity deals with the superelastic response of SMA under an applied mechanical load, which describes its so-called rubber-like behavior. Stress induced martensite is a post product of such loading situation. We initiate loading while the material temperature is above austenitic finish temperature where a stable parent phase exists. A great deal of transformation strains are attained and these stains can be completely restored once unloading process is complete as long as material was not plastically deformed. This kind of behavior can be utilized for applications in which temperature variations are not possible. The strains generated are high enough to make the use of SMAs in devices where hydraulics systems are applicable,

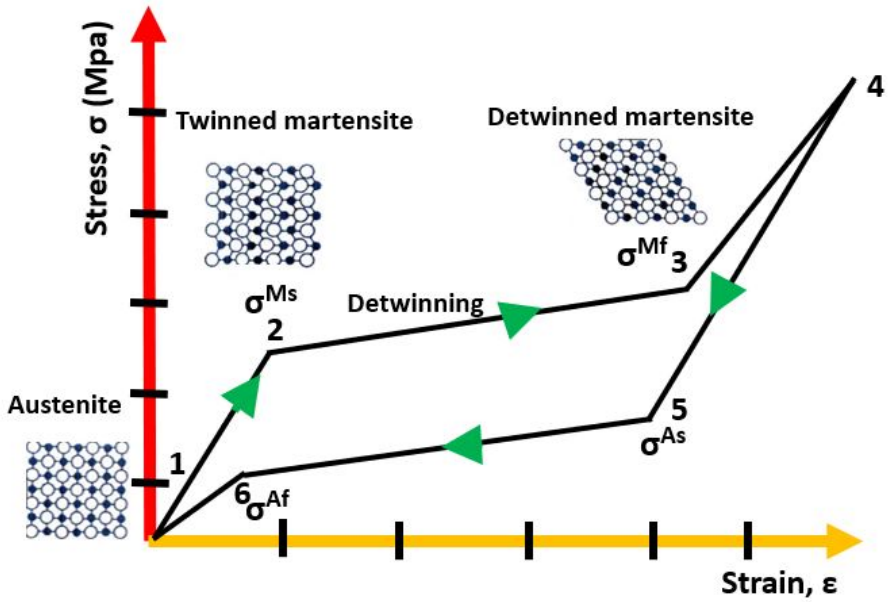

Figure 5: Stress-Strain schematic to show Pseudoelastic behaviour of SMAs.

but lightweight systems are required. To better explain this phenomenon, we can see how pseudoelastic behavior shows a hysteric response on a stress-strain space.

By following a load-unload path under mechanical stimuli, we attain hysteresis in stress-strain plateau, which can be seen in Figure 5, initially when the load is applied we are in the stable parent phase and material deforms elastically from 1 to 2 with a slope of value equivalent to austenitic young's modulus, at 2, it hits the critical stress value, which shows the onsite of phase transformation from austenite to martensite, which is denoted by (σ^{MS}) and if we consider the phase diagram, the loading path has hit the surface for initiation of martensitic transformation. From 2 to 3, we can observe that a lot of strains have been generated, which are termed as transformation strains and (σ^{MF}) marks the completion of the martensitic transformation. Now, further loading will deform the material elastically, but the slope from 3 to 4 will follow a value equivalent to martensitic young's modulus of the material, if we keep

on loading, the material will start to deform plastically and since it's an irreversible property we won't be able to recover all the strains generated thus far. Now, if we relax the load and start unloading it will follow an elastic trend from 4 to 5 until it hits the austenitic start surface in the phase diagram, which is denoted by (σ^{AS}), here reverse transformation begins and continues from 5 to 6 and marks the completion where stresses reach (σ^{AF}) in between these points all transformation strains are fully recovered. The material is then elastically unloaded to 1.

End of this section unfolds the basics of SMAs and its properties. A major aspect of this work is based on fracture mechanics and its general concepts will be discussed in coming sections.

1.3 Fracture mechanics of SMAs

As mentioned above, SMAs are a complicated group of intermetallic materials. Their ability to transform from one phase to another by employing shear lattice distortion, twinning, detwinning, and reorientation of martensitic variants and achieving large amounts of transformation strains adds to the complexities faced while dealing with fracture mechanics of these materials. Fracture behavior of these materials is not straight forward due to their strong thermo-mechanical coupling, ability to reverse transform, and possible generation of transformation induced plasticity (TRIP). Existing fracture mechanics concepts do not address these subjects and it's questionable to follow fracture toughness approach devised for elastic and elastic-plastic materials without adequate changes. In this section, theoretical, numerical, and experimental work in the field of fracture toughness evaluation of phase transforming materials under isothermal and isobaric loading is addressed, as well as failure mechanisms of SMAs.

1.3.1 Micro-mechanisms of fracture mechanics of SMAs

When we compare SMAs with other intermetallic alloys, the failure mechanism of SMAs is quite different. These intermetallic alloys fail due to cleavage [179], which classifies them as brittle materials. SMAs behavior is far more complex owing to diffusionless solid-to-solid recoverable phase transformation, orientation and/or reorientation of martensitic variants. Since these processes start at lower stress values, they can delay and/or hinder the cleavage process. Because these complex processes can act simultaneously in SMA (such as NiTi), it has been observed that ductile tearing and cleavage fracture often coexist at the same time as shown in Figure 6, leading to its failure [50, 121].

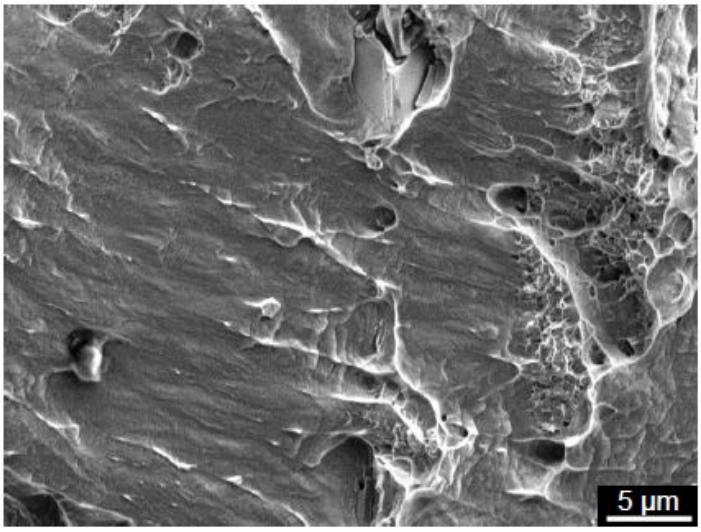

Figure 6: In-situ SEM image of a pseudoelastic NiTi demonstrating different fracture mechanisms observed from the fracture surface (After [50]).

There is a strong dependence on the microstructure in a way that the presence of precipitates, their size, their distribution, and their volume fraction, governs how one failure phenomena will dominate over the other [27]. Experimental and numerical studies have shown that by changing the size of the precipitates, oxides, and

carbides in the microstructure of SMAs, material's properties can be tuned. Optimized material strengths can be achieved [50] and required transition temperature can be accomplished by using heat aging treatments [48, 82]. Fractography of failed sample showed that both cleavage planes and dimples co exits on the fracture surfaces of SMAs, which points out that the failure mechanism is quasi-cleavage *i.e.*, there is possible void growth and its coalescence but failure is majorly dominated by cleavage [98]. In situ SEM images have revealed that the fracture mechanism makes transitions from ductile to brittle when grain size is reduced down to nanoscale [1]. Larger grain size have shown the presence of dimples on the fracture surfaces and failure happens due to ductile tearing instead of cleavage.

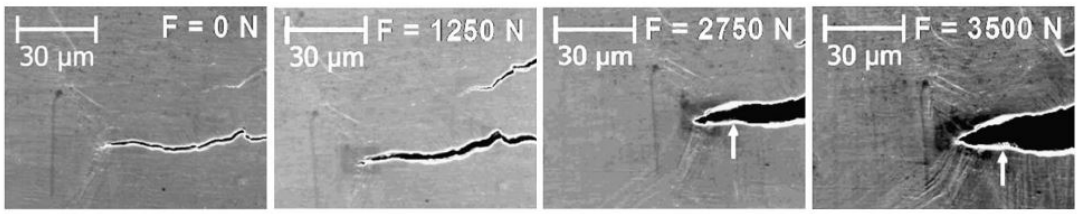

Figure 7: In-situ SEM images of a pseudoelastic NiTi SMAs at different applied load levels during a fracture experiment (After [54]).

In the fracture toughness experiments, it was observed that crack tip blunting is not prominent before crack growth in pseudoelastic NiTi alloys [54]. While examining in-situ SEM images Figure 7, crack tip remained sharp which points out that there is not enough plastic deformation close to crack tip [159] before crack starts growing, which can be attributed to large martensitic transformation zones created at the vicinity of the crack that indeed hinders plasticity. Before the cracks start to grow, non-linearity [57] is observed in the load vs load-line displacement curve, which may be a sign of void growth and coalescence caused by phase transformation. Numerical studies are required to study the effects of phase transformation on void nucleation,

void growth, and coalescence.

1.3.2 Experimental investigation on fracture toughness of SMAs under mechanical loading

The American Society for Testing and Materials (ASTM) have managed to compile standards to experimentally evaluate fracture toughness of elastic and elastic-plastic materials [4]. These standards provide guidelines to select an appropriate fracture toughness parameter for certain conventional structural metals, and escorts toward the right methodology to be used to measure those parameters. In the realm of SMAs, NiTi alloys are most extensively researched material when it comes to understand fracture response through experimental investigations. The initial studies focused on evaluating fracture toughness values of NiTi alloys, were based on assertion that Linear Elastic Fracture Mechanics (LEFM) is a valid approach [161, 54, 140]. These experiments were done on pesudoelastic, austenitic, and martensitic SMAs with test specimens not large enough to make sure that small scale yielding constraints are satisfied. They all found a critical stress intensity factor of about 30 [Mpa.m$^{1/2}$]. These results not only suggested that failure response of such materials is 'only brittle' but also missed on many prerequisites and validity conditions, where thickness constraints were not satisfied as the plastic zone close to crack tip calculated from those results were not approximately equivalent to $2.5(K_{Ic}/\sigma_y)^2$.

In order to visualize what happens near the crack tip, in-situ synchrotron X-ray diffraction experiments [33] were performed, which highlights some of the main insights. For SMAs, the size of detwinned martensite zone should be considered instead of the size of the plastic deformation close to the crack tip, to satisfy size restrictions and small-scale yielding criteria. High tensile strains were observed at the vicinity of the crack due to stress induced martensite, but these strain fields become

compressive upon unloading, which is not the case with irreversible plasticity. Due to the non linearity in the deformation response, these above findings questioned LEFM as an effective method for calculating the fracture toughness of SMA. Another backlog of using LEFM and using K_{Ic} as the single fracture toughness parameter for superelastic alloys was that they show monotonic dependence on temperature as shown in Figure 12, which questions the validity of K_{Ic} as material independent fracture toughness parameter.

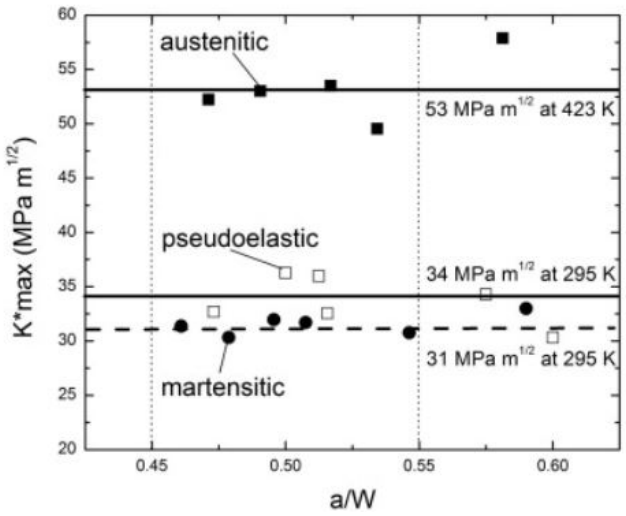

Figure 8: Comparison of K^*_{max} for martensitic (filled circles), superelastic (open squares) and austenitic (closed squares) NiTi SMAs with different initial crack lengths (After [54]).

The SEM images from the experimental investigation on pseudoelastic SMAs [54, 55] suggested that crack tips for NiTi stay sharp instead of getting blunt. Blunting is a process where crack faces move apart before crack starts growing, as observed in conventional ductile materials, which is associated with dislocation processes. This questions the suggested methodology for creating R curves, which will be discussed in the coming sections. Along with this evidence, infrared thermographic images helped to observe temperature variations on the material's surface, which can indicate

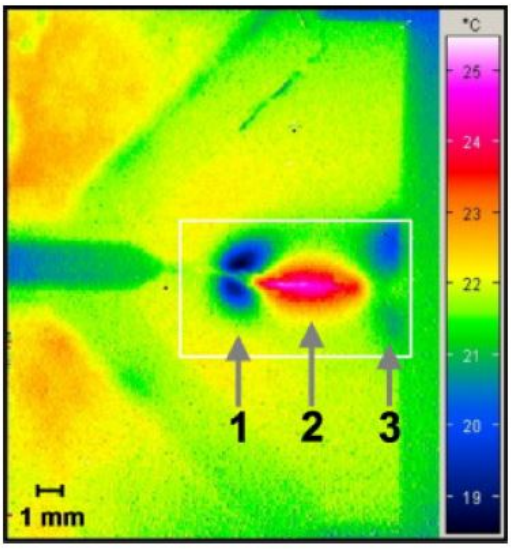

Figure 9: Thermographic image while testing NiTi SMA specimen. 1 refers to crack tip position prior to crack propagation, 2 refers to the actual crack position , and 3 refers to a region ahead of the crack tip (After [55]).

heat flows associated with martensitic forward and reverse transformations. Since reverse transformation is an endothermic process, Figure 9 provides direct physical evidence for the reverse transformation of stress-induced martensite in the material regions left behind the advancing crack tip expected to occur due to unloading in that region. Now, this raises questions about the effectiveness and accuracy of the unloading process required to calculate material compliance during fracture toughness experiments.

1.3.3 Analytical and numerical investigations on the size of transformation zone near the crack tip

Apart from aforementioned experimental findings there has been ample effort invested to analytically and numerically find closed form expressions that can determine the size of stress-induced transformation zone close to crack tip. These closed form expressions can be used to satisfy validity conditions for initial thickness and initial

crack length for the specimen under test, which are required to make sure calculated fracture toughness values can be accepted. But most of the analytical and numerical work [109], [106] could not completely determine the size of the transformation zones. Their work did not include possible plastic yielding and stress-strain hysteric nature of SMAs. Indeed, the results shown in Figure 10 are not able to capture experimental strain maps properly.

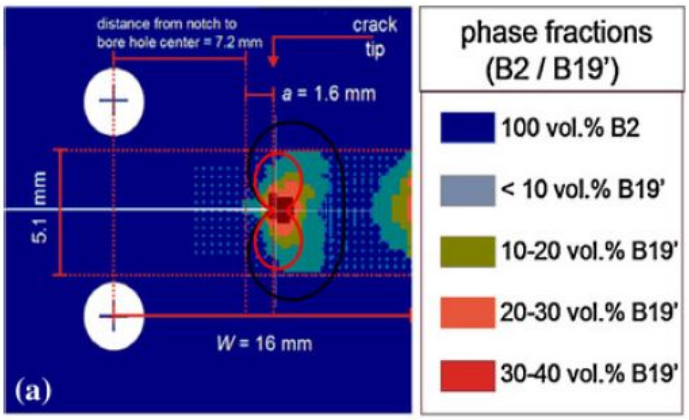

Figure 10: Experimental evidence of transformation zones close to crack tip using in-situ X ray diffraction and red and black mark showing plane stress and plane strain transformation zones (After [109, 106]).

Others did not care to include stress redistribution caused due phase transformation at the vicinity of the crack [94], and many others based their work on the findings of Irwin's correction of LEFM [22], missed capturing the experimental results accurately. A recent model [9] which included plastic yielding and also incorporated stress redistribution close to crack tip, showed that more load will be required for plastic zones to appear at crack tip, thus plastic zones for phase transforming materials tend to be small as compared to conventional elastic-plastic materials Figure 11 and validation conditions should be based on size of detwinned and/or reoriented martensite zones rather than inelastic zones.

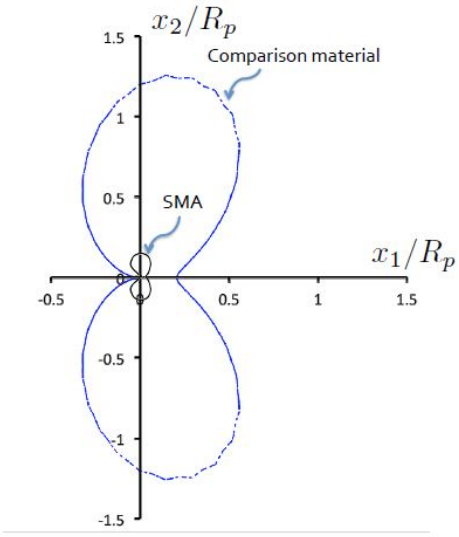

Figure 11: The inner curve represent the plastic zone boundary in an SMA material under mode I loading and the outer one the plastic zone boundary of the SMA without accounting for phase transformation (After [9]).

1.3.4 Computational and theoretical investigations on isothermal fracture toughness of SMAs using J-integral and Elastic Plastic Fracture Mechanics (EPFM)

Initial numerical studies showed that there is load path dependence on the size and shape of transformation zones [168] and the formation of stress-induced martensite tend to relax stresses close to crack tip. Following the insight, further studies suggested that more load will be required to invoke plastic yielding as the martensitic transformation is a dissipative process, which resulted in decreasing maximum normal stresses in that region [164, 166]. This response tends to have an impact on slow and stable crack growth of SMAs and the resulting resistance curves.

Numerical analysis conducted to check J-integral's validity as a material independent fracture toughness parameter for pseudoelastic SMAs [9], pointed out that

for mode-I loading J-integral is path-dependent. Comparison between far-field J_∞-values and crack-tip J-values Figure 12 suggested that the difference between these values is not as prominent as it is observed in elastic-plastic materials and the assumption that states that the fracture toughness calculations of SMAs can be based on path-independence of J-integral is acceptable.

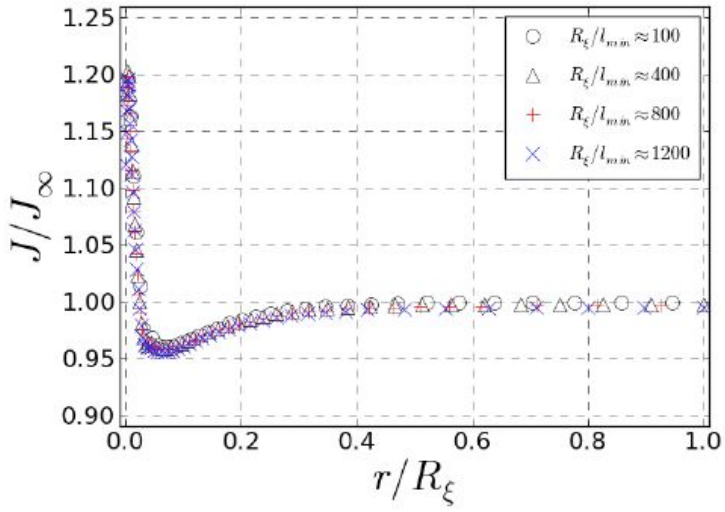

Figure 12: J-integral values vs the radius of the circular integration contour for mode I loading. The markers correspond to different load levels represented by the size of the corresponding transformation zones R_ξ. J_∞ is the far-field J-value (After [9]).

Mode-I and mixed-mode numerical experiments to evaluate fracture toughness of SMAs, where volumetric strains were avoided and only shear strains were considered [175, 177], suggested that phase transformation causes an overall enhancement in fracture toughness of these materials. Theoretical work [173] where the combined effect of shear and volumetric transformation strains were studies showed adherence to the numerical results and suggested that shape of the stress-strain hysteric response of SMAs is important to quantitatively determine transformation toughening

of the material. They also suggested that factors such as mismatch in young's moduli, slopes of stress-strain curves during transformation, and amount of reverse phase transformation in the wake of growing crack will impact transformation toughening.

Transformation toughening due to phase transformation is a phenomenon that provides additional resistance to crack growth. However, there is no experimental evidence to dispel doubts about the enhancement or abatement effects associated with reverse phase transformation. Finite element analysis with a model that works on an assumption of null or full transformation [153], instead of partial reverse phase transformation which is observed experimentally, suggested that reverse transformation reduces toughening effect. Cohesive zone model analysis [45] which only works for proportional loading agreed to similar conclusions. Numerical analysis for quasi-static steady state crack growth [16] were free of any assumptions and showed that due to the dissipation of energy caused by reverse transformation, there is a contribution towards the enhancement of transformation toughening. These results under the finite element framework lack to fully capture the reality and raise more questions than giving adequate answers, and indeed an experimental evidence is required to conclude not so obvious phenomenon.

1.3.5 Stable crack growth under isobaric actuation

There is a limited amount of effort invested in the experimental evaluation of fracture toughness of SMAs under isobaric actuation. The double-notched NiTi specimens [65] were examined under a constant tensile load much lower than the isothermal strength of these materials, and thermal cycling was applied. Due to the unstable crack propagation during the first few cooling cycles, the specimen failed, which may be due to the global induced martensitic transformation. Pre-cracked, compact tension specimens under bias a load and actuation cycles showed stable crack growth

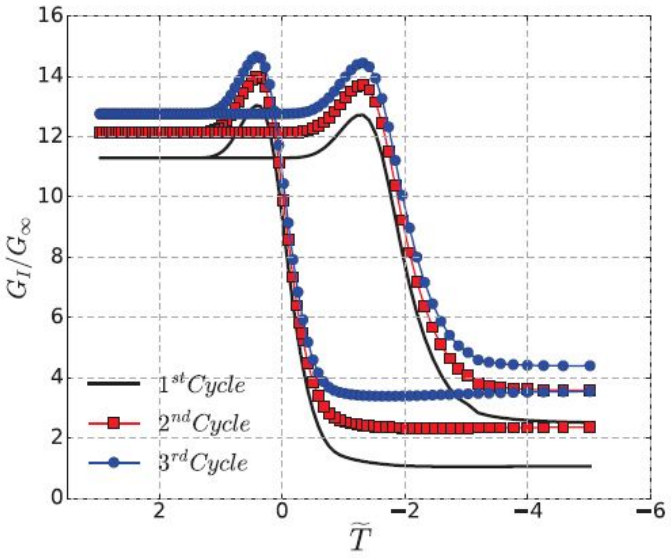

Figure 13: Evolution of the normalized crack-tip energy release rate, G_I/G_∞, versus uniform normalized temperature, T, showing higher levels of the driving force due to accumulation of TRIP (After [74]).

during multiple heating-cooling cycles [76]. In these experiments, crack growth was observed during the cooling part of thermal cycles rather than during the heating phase and no crack growth was observed once phase transformation was complete.

Numerical analysis were carried out [20, 74] to study the impact of thermo-mechanically-induced transformation on the resistance to growth and fracture toughness enhancements associated with it. Phase transformation and TRIP were found to affect the driving force for crack growth. Accumulation of TRIP in regions in front of the crack tip over cycling and global phase transformation during cooling, may (eventually) raise the driving force required for crack growth above a material specific "critical" value that is usually responsible for crack growth. Figure 13, where it is clearly observable that the driving force ratio has shown a noticeable increase in 3^{rd} cycle when compared to the 1^{st} cycle. Transformation and TRIP strains not only demands for higher load levels for stable crack growth but due to irreversible nature of

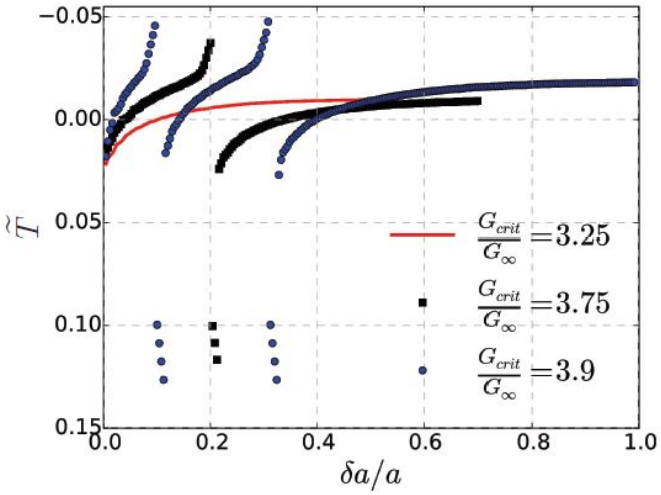

Figure 14: Normalized temperature, vs. normalized crack growth, showing the crack resistance "-curve" behavior for varying bias loads. The higher the ratio G_{cr}/G_∞, the smaller the bias load (After [71]).

plasticity, it provides a shielding effect because of their presence in the wake of growing crack. Figure 14 shows critical energy's dependence on applied bias load levels for crack growth during isobaric experiments. Depending on the bias load, either there is no crack growth or crack growth ceases once the whole material is transformed or steady-state crack growth conditions are achieved during cooling in the first thermal cycle.

1.4 Motivation for this research

Since their discovery, the SMA industry has been dominated by products for biomedical applications with geometrically small feature sizes, especially endovascular stents. In regard to the demands and requirements, these products were geometrically small and perform on low service loads thus technological importance of fracture mechanics was limited to prevent crack nucleation rather than controlling crack growth. Later, with advancements in technology and an increased demand for SMAs in commercial actuation for large aerospace devices, vibration damping in humongous structures, energy conversion, and storage in the automotive industry, to name a few, proper understanding of fracture mechanics concepts to ensure safe practice was encouraged.

1.4.1 Proposed modifications to ASTM standards for experimental measurement of fracture toughness

- A mechanics-aided test method for measuring the fracture toughness of SMAs, whose deformation/failure response violates basic assumptions of ASTM standards for measuring fracture toughness in conventional ductile materials, has been recently proposed. The proposed methodology relies on the resistance curve format of ASTM standards but differs from it in the determination of the elastic part of the J-value, both for stationary and advancing cracks, in an effort to accommodate the transformation/orientation-induced changes in the apparent elastic properties. Detailed discussion of this proposed modifications to ASTM standards are required, to account for the expected degree of improvement in the measurement accuracy, the need for further ones regarding the uncertainty as to where to specify the fracture point on the obtained resistance curve, the specimen thickness requirement to ensure a conservative, constraint-independent measurement, and the temperature dependence of the

measurements.

1.4.2 "Reversible" phase-transformation-induced fracture toughness enhancement

- As already mentioned, SMAs display slow and stable crack extension, *i.e.*, an R-curve behavior, which is attributed mainly to phase transformation as opposed to plastic deformation in conventional ductile metals. The observed toughening (stable crack growth) is due to irreversibility effects associated with nonproportional straining in the active phase transformation zone and the shielding effect of the transformed material left in the wake of the advancing crack. The effect of the reversibility of phase transformation on the fracture toughness enhancement is examined experimentally to (i) demonstrate that the toughness enhancement due to crack advance in SMAs may be "reversed" by partial unloading, which has implications on the evaluation of the resistance curve and its validity conditions, and (ii) provide an experimental verification of the theoretical insight into the mechanics of stable crack growth.

1.4.3 Experimental fracture toughness measurement under actuation loading

- SMAs are desirable in actuation applications that involve thermal sweeps. A single-parameter description of driving force for crack growth is proposed for actuation loading conditions on the basis of a path-independent contour integral, which collapses to the J-intgral under isothermal conditions. Experimental measurements of the fracture resistance of SMAs under actuation loading conditions are reported. The obtained results represent the first experimental measurement of the fracture toughness of SMAs under coupled thermo-mechanical

loading, and indicate that the fracture toughness enhancement associated with crack advance under isobaric thermal loading is less pronounced than the corresponding one under isothermal mechanical loading.

1.4.4 On the relative importance of cleavage and ductile tearing

- Although SMAs belong to a relatively brittle class of materials, that of intermetallics, their fracture surfaces are characterized by both cleavage and dimples, with the latter being indicative of ductile rupture. Two clear differentiators of SMAs from other intermetallics, which may contribute to the presence of ductile rupture are their ability to transform their crystallographic structure and the presence of precipitates in large volume fractions. Numerical simulations are required in an effort to quantify the relative importance of the two fracture mechanisms in the overall failure response of these materials. The numerical approach adopted includes a single pre-existing void, assumed to have initiated from a second phase particle, embedded in a SMA matrix material. These unit cell studies allow for an investigation of void growth and coalescence, ignoring void formation and its footprint in the subsequent microstructure evolution.

2 Notes on the experimental measurement of fracture toughness of SMAs.

Fracture toughness is a generic term regarding material resistance to crack advance. The experimental measurement and standardization of fracture toughness, understood here as a constraint-independent material parameter both as a critical point or as a resistance curve, is imperative in the application of fracture mechanics methods to structural integrity assessment, damage-tolerance design, performance evaluation, and quality assurance, among others. Therefore, fracture toughness testing and evaluation is of out most importance in fracture mechanics and its engineering applications.

.

2.1 Valid ASTM standards for phase transforming materials

In this chapter a methodology, recently proposed for measuring the fracture toughness of SMAs whose deformation response violates basic assumptions of the current ASTM standards, is discussed [58]. The proposed methodology relies on the resistance curve format of the [4], developed for conventional ductile materials, which is based on concepts of elastic-plastic fracture mechanics, employing the J-integral as the fracture criterion. SMAs display an R-curve behavior, *i.e.*, slow and stable crack extension, which is due to transformation-induced toughening rather than plastic deformation-induced as in the case for conventional ductile materials, and fracture predominantly through cleavage rather than ductile void growth and coalescence [14, 142, 54, 20, 160]. The requirements on specimen sizes for J-dominance are much less strict compared to those for K-dominance, where K stands for the stress intensity factor in LEFM. LEFM requires the zone of non-linear deformation close to the crack tip, regardless of the mechanism, to be just a small fraction of the characteristic dimensions of the

specimen. With respect to SMAs, this restriction leads to a requirement on the size of the transformation (or orientation of self-accommodated martensite in case of martensitic materials) zone being small enough for LEFM to be valid. For such a requirement to be satisfied, the SMAs specimens may be prohibitively large.

The proposed method differs from ASTM standards E1820 the [4] in the determination of the elastic part of the J-value, J^{el}, in an effort to account for the mismatch among the apparent elastic properties of austenite, self-accommodated, and oriented martensite. J^{el} is calculated by multiplying the elastic area under the load–load line displacement curve with a configuration-dependent factor. The range of error in the fracture toughness measurement introduced by the proposed method and ASTM standards E1820 [4], the uncertainty as to where to specify the fracture point on the obtained resistance curve, the specimen thickness requirement to ensure a constraint-independent measurement, and the measurements' dependence on temperature are discussed.

2.2 Review of recently proposed test method

2.2.1 Measurement of J-integral for stationary cracks

The expression utilized for the measurement of the J-values is given first for stationary cracks and for advancing cracks subsequently.Both expressions rely on the elastic compliance slope measured during partial unloading–reloading paths for distinguishing between their elastic and inelastic components.

The J-value is calculated from the load–load line displacement record of a Compact Tension (CT) specimen (Fig. 18(a)) as

$$J = J^{el} + J^{in} = \frac{\eta^{el} A^{el}}{Bb} + \frac{\eta^{in} A^{in}}{Bb}, \tag{1}$$

where B is the specimen thickness, $b = W - a$ is the length of the unbroken ligament (W is the specimen width and a the crack size). A^{el} and A^{in} are the elastic and inelastic components of the area under the load–load line displacement curve, respectively (Fig. 18(b)). η^{el} and η^{in} are geometry-dependent factors, the existence of which is discussed in [58].

2.2.2 Measurement of J-integral for advancing cracks

The expression for the J-integral given above, Eq. (1), is valid only for constant crack length, a. For advancing cracks, an incremental formulation is needed [41]

$$J_i = J_i^{el} + J_i^{in},$$

where J_i^{el} and J_i^{in} are evaluated from the previous step

$$J_i^{el} = \left[J_{i-1}^{el} + \frac{\eta_{i-1}^{el}}{B b_{i-1}} A_{i-1,i}^{el} \right] \left[1 - \frac{\gamma_{i-1}^{el}}{b_{i-1}} (a_i - a_{i-1}) \right], \tag{2}$$

and,

$$J_i^{in} = \left[J_{i-1}^{in} + \frac{\eta_{i-1}^{in}}{B b_{i-1}} A_{i-1,i}^{in} \right] \left[1 - \frac{\gamma_{i-1}^{in}}{b_{i-1}} (a_i - a_{i-1}) \right]. \tag{3}$$

Above, $A_{i-1,i}^{el}$ and $A_{i-1,i}^{in}$ are the increments of the elastic and inelastic areas under the load–load line displacement record from step $i-1$ to i, respectively:

$$A_{i-1,i}^{el} = \frac{1}{2}(P_i + P_{i-1})(\delta_i^{el} - \delta_{i-1}^{el}), \tag{4}$$

and,

$$A_{i-1,i}^{in} = \frac{1}{2}(P_i + P_{i-1})(\delta_i^{in} - \delta_{i-1}^{in}), \tag{5}$$

where $\delta_i^{el} = P_i C_i$ and $\delta_i^{in} = \delta_i - \delta_i^{el}$ are the elastic and inelastic components of the

displacement (Fig. 18(c)) and C_i is the unloading elastic compliance. γ^{el} and γ^{in} are geometry-dependent factors and can be determined using η^{el} and η^{in}, respectively [58].

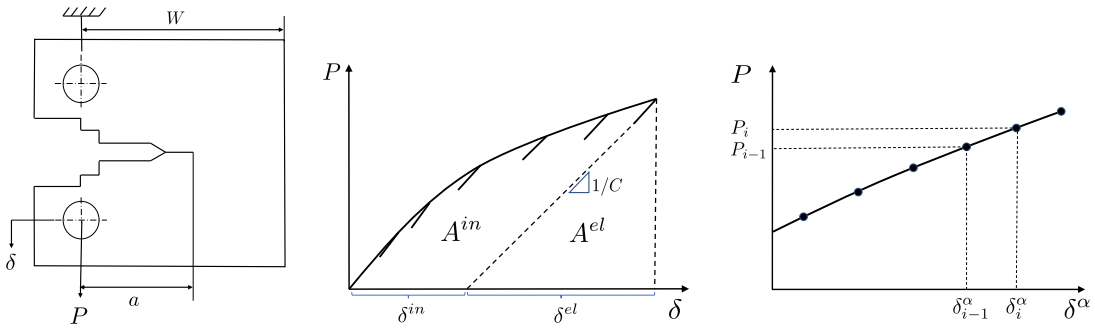

Figure 15: Schematic representation of (a) CT specimen with crack size a and width W; (b) δ^{el}, δ^{in}, A^{el} and A^{in} on a load-displacement curve; (c) definition of the incremental elastic/inelastic area from step $i-1$ to i. δ^{α}stands for either δ^{el} or δ^{in}.

2.2.3 Calculating crack size

To measure crack extension, the elastic compliance method, a widely used technique [29, 78], is proposed, in accordance to [4].

2.2.4 J_R-curve and J_{I_C}

Once J and Δa values are known, the J_R-curve can be constructed, following the [4] procedure. A construction line is first plotted from the origin with a slope of $M\sigma_Y$, where M is a scalar and σ_Y is the effective yield strength, *i.e.*, the average of the critical stress, σ_{cr}, and the ultimate tensile strength, σ_{TS}. σ_{cr} denotes either the stress required for initiation of phase transformation or orientation of self-accommodated martensite depending on whether the material is in the austenite or self-accommodated martensite state at zero load, respectively. The slope of the construction line is intended to represent the component of crack extension that is due to crack blunting, as

opposed to tearing. The default value is $M = 2$. Two exclusion lines are then drawn parallel to the construction line intersecting the abscissa at 0.15 mm and 1.5 mm. J-Δa data points that fall between these two exclusion lines are plotted and a power-law regression is fit throughout. To determine the J_{I_C} fracture toughness, an offset line is then plotted parallel to the construction line, intersecting the abscissa at 0.2 mm. The intersection of the 0.2 mm offset line and the regression line defines an interim value of the J-integral. This interim value is considered a conservative, constraint-independent fracture toughness value if the qualification requirement, $B > 10\, J_{I_C}/\sigma_Y$, related to the specimen thickness is met. Fig. 16 shows a typical J_R-curve together with the definition of lines and region of qualified data.

2.3 Discussion of the proposed test method

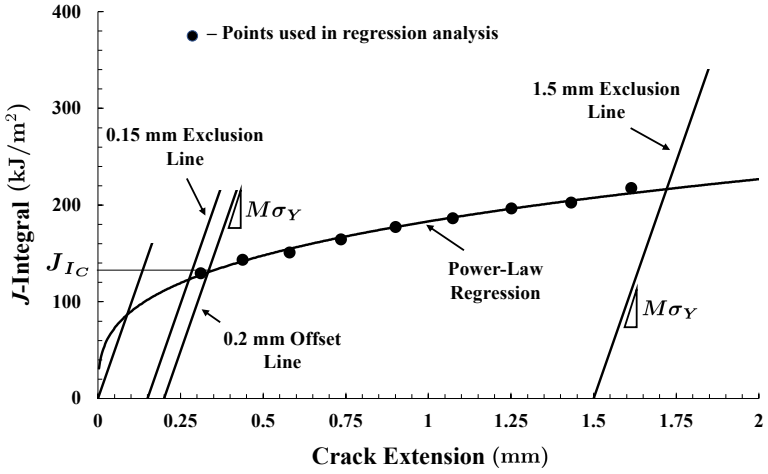

Figure 16: Definition of construction lines and region of qualified data for constructing the J_R-curve and determining J_{I_C}.

Crack growth in SMAs invariably involves elastic unloading, martensite reorientation and non-proportional plastic deformation near the crack tip. The J-integral is

based on nonlinear elasticity which inadequately models these aspects of deformation. However, under J-controlled crack growth conditions [63], which require nearly proportional inelastic deformation everywhere but in a small neighborhood of the crack tip, the J-integral can still be used to analyze crack growth. The condition for J-controlled crack growth may be expressed as

$$\omega = \frac{b}{J}\frac{dJ}{da}, \tag{6}$$

where according to [63], ω should be of the order of 40.

2.3.1 Measurement of J-integral

In conventional ductile materials, J^{el} is calculated by taking advantage of the relationship between the energy release rate, G, and the tabulated expressions of the stress intensity factor, K, as a function of crack configuration and load,

$$J^{el} = G = K^2/E', \tag{7}$$

where $E' = E$ for plane stress and $E' = E/(1-\nu^2)$ for plane strain, and ν is the Poisson's ratio. The above expression is not valid for SMAs, for which the Young's modulus, E, assumes different values for austenite, self-accommodated, and oriented martensite. In the proposed methodology, J^{el} is evaluated by multiplying the elastic part, A^{el}, of the area under the load–load line displacement record with a configurational-dependent factor η^{el} according to (1) for stationary cracks. In this expression, the transformation/orientation-induced changes in the apparent elastic properties are taken into account through A^{el}. For advancing cracks, a correction is further needed and J^{el} may be calculated according to (2), in which

$\gamma^{el} = \eta^{el} - 1 - \frac{b}{W}\frac{\left(\eta^{el}\right)'}{\eta^{el}}$, where $\left(\eta^{el}\right)' = d\eta^{el}/d(a/W)$ [58, 182, 183]. Although the correction of J-values for crack advance is of little consequence for the measurement of the point fracture toughness, J_{I_C}, is of considerable one for stability analysis; instability is expected when the crack driving force J-curve is tangent to the J_R-curve [128], *i.e.*,

$$J(P, a) = J_R(\Delta a), \tag{8a}$$

$$\frac{dJ(P, a)}{da} = \frac{dJ_R(\Delta a)}{da}, \tag{8b}$$

and thus the slope of the J_R-curve at a given amount of crack extension is indicative of the relative stability of the crack growth. A material with a steep J_R-curve is less likely to experience unstable crack propagation.

2.3.2 Elastic area under the load–load line displacement record, A^{el}

A^{el} is determined using the compliance of the CT specimen obtained by partial unloading–reloading paths. Due to transformation hysteresis or the irreversibility of orientation, unloading initially results in a linear load–displacement response. The inverse of this line's slope, *i.e.*, the compliance, is dependent on the crack configuration and the "effective" elastic response of the specimen (austenite plus regions of oriented martensite or self-accommodated plus oriented martensite depending on temperature). The elastic part of the load–displacement area is determined by extending this straight line to meet the abscissa, *i.e.*, the displacement-axis. In the case of orientation, the so-determined area is related to the energy that can be recovered upon unloading, given that upon unloading reorientation is not appreciable; mode I loading is nearly proportional. In the case of phase transformation, however, unloading may result in reverse phase transformation and further release of stored energy.

In any case, the defined area corresponds to the component of the load–displacement area related to the elastic deformation during loading and not necessarily to the part that can be recovered upon unloading.

2.3.3 J_R-curve values measured from the proposed approach vs ASTM standards

In Figure 17, the J_R-curves constructed by the proposed method and ASTM standards are depicted for one of the experiments performed in [58] at temperature, $T = 80$ °C, at which the material's stable phase is austenite and phase transformation to stress-induced oriented martensite close to the crack tip takes place during loading. As it can be seen in the figure, the J_R-curve values corresponding to the proposed method are higher than those corresponding to ASTM standards at the initial stages of crack extension and become lower as the crack extends further. This trend has been observed in all experiments: Given that the inelastic part of the J-integral is the same in both methods, the differences in the J-values are due to differences in the elastic part, J^{el}. Looking at the expression of J^{el}, Eq. (7), for static cracks, the ASTM J^{el}-values are expected to be lower than the J^{el}-values resulted from the proposed method; the proposed method accounts for the change in the apparent elastic properties close to the crack tip, which result in an "effective" Young's modulus of a lower value, given that the apparent elastic modulus of oriented martensite is smaller than that of austenite. During crack advance, the corrected J^{el}-value (Eq. (2)) increases slower than the ASTM J^{el}-value due to the second term in the equation, and eventually the J_R-curve values of the proposed method fall below the ASTM ones.

In order to further investigate the error in the J_{I_C}-measurement introduced by the proposed methodology and [4], finite element analysis is undertaken (see Appendix7.1). Since the difference between the two methodologies is limited to the calculation of J^{el},

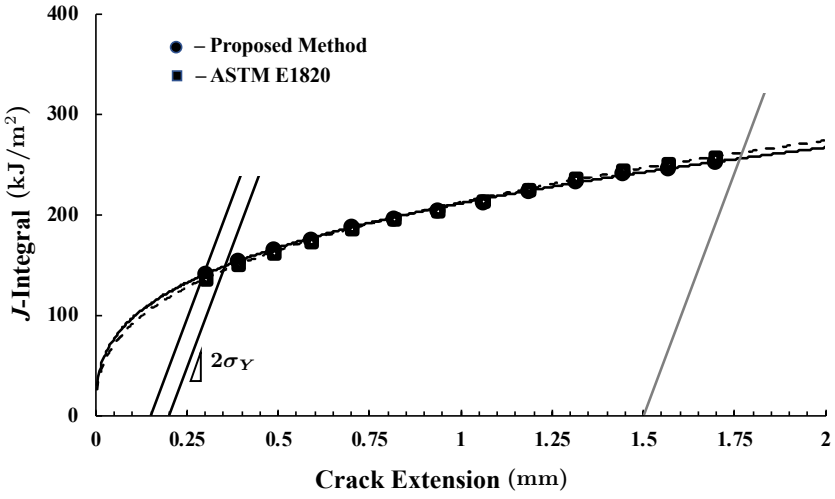

Figure 17: J_R-curves obtained from the proposed approach and [4] for one of the experiments performed in [58] at temperature, $T = 80$ °C.

the constitutive model adopted only accommodates the change in the elastic properties in the absence of transformation or orientation strains (Fig. 18[a]). The J-value is calculated from the load–load line displacement record using the proposed methodology and the ASTM standards, and through the domain integral method, described in [129, 95, 149]. As it can be seen in Fig. 18[b], the proposed methodology gives J-values in close proximity to the those obtained from the domain integral method, while the error introduced following the ASTM standards is significant. These calculations assume that the ratio between the Young's moduli of austenite and martensite is 2.3, a value which should be considered among the highest observed in NiTi [89]. Given the error in J^{el} introduced by [4] and $J^{el} \approx 0.4J^{in}$ at J_{I_C}, at least for the experiments performed, the error expected using the ASTM standards in determining J_{I_C} should be no more than 7–10%.

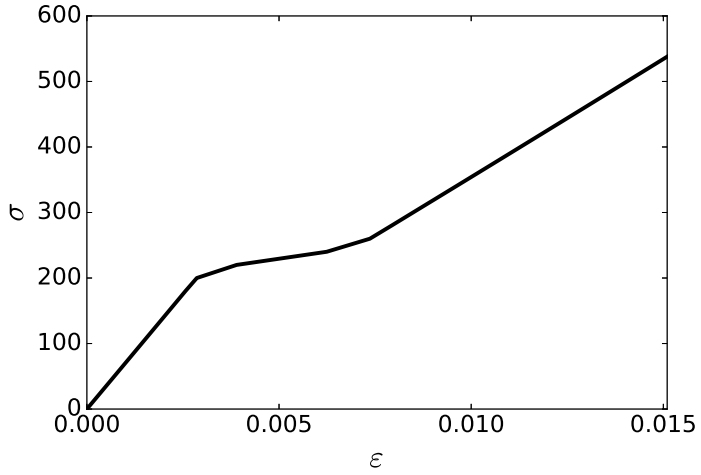

[a]

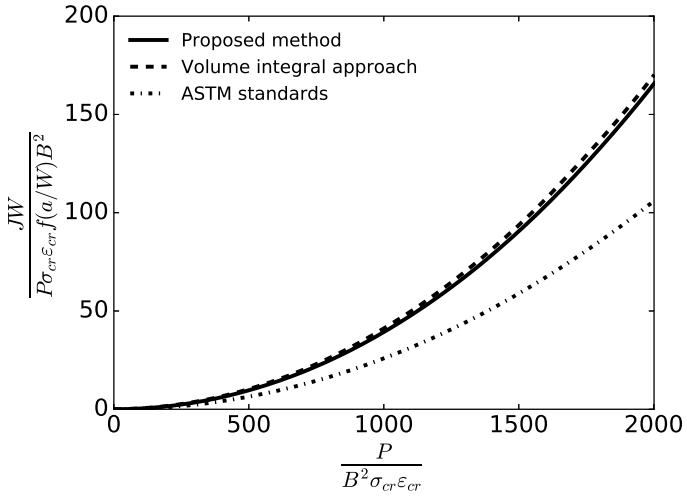

[b]

Figure 18: Figure[18.a] refers to the uniaxial stress vs strain response of the non-linear elastic law and Figure[18.b] refers to Normalized J vs normalized load .Normalized J-values calculated .

2.3.4 Calculation of crack size

According to the elastic compliance method, the crack size can be measured by the following formula:

$$\frac{a}{W} = 1.000196 - 4.06319u + 11.242u^2 - 106.043u^3 + 464.335u^4 - 650.677u^5, \quad (9)$$

where $u = 1/\left(\sqrt{BEC}+1\right)$ and C is the unloading elastic compliance. A good agreement between the elastic compliance calculations and optical measurements was found in [58], which can be explained by the mild dependence of the above formula on E since the elastic compliance scales with the inverse of E. Note that in the elastic compliance calculations, E was assumed equal to the Young's modulus of the stable phase at the nominal temperature at which the experiments took place.

2.3.5 Determination of fracture toughness, J_{I_C}

The default slope, $2\sigma_Y$, of the construction line approximates the apparent crack advance due to crack-tip blunting when there is no slow stable crack tearing under the assumption that, before tearing, the crack advance is equal to one half of the crack-tip opening displacement. In SMAs, crack-tip blunting is not as pronounced as in conventional ductile materials and such an assumption is an exaggeration [54].

According to [4], the obtained J_{I_C}-values should satisfy the requirements, $b, B > 10\ J_{I_C}/\sigma_Y$, which ensure J-dominance and constraint-independence, respectively. In conventional ductile materials, the apparent thickness dependence in fracture toughness reflects the differing relative contributions of two distinct fracture mechanisms, flat vs shear fracture, due to crack tunneling and shear lip formation. In thick specimens, flat fracture mechanism dominates, and further increases in thickness have relatively little effect on the measured toughness. SMAs, however, fail predominantly by

cleavage fracture and do not form tunnels and shear lips. Cleavage fracture toughness is known to exhibit a slight thickness-dependence due to weakest-link sampling effects. Thus, the aforementioned thickness requirement for conventional ductile materials is far more stringent than is necessary to ensure a thickness-independent fracture toughness measurement in SMAs. A test matrix of fracture experiments on specimen with various thicknesses is needed for the rigorous relaxation of the thickness requirement. The corresponding requirement on the in-plane dimension $b > 10\ J_{I_c}/\sigma_Y$, should still be enforced to ensure J-dominance on the stress and strain fields in the vicinity of the crack tip.

2.3.6 On the temperature dependence of the fracture toughness measurements

[4] and the proposed methodology assume isothermal quasi-static loading conditions. The isothermal assumption in SMAs is valid for a range of strain rates within the regime of quasi-static processes even for complex geometries and loadings despite the generation or absorption of latent heat during phase transformation (forward transformation from austenite to martensite entails generation of heat and reverse phase transformation absorption of heat). At higher strain rates, depending on the geometry, convective boundary conditions and associated heat transfer, the generation or absorption of latent heat may have a strong impact on the deformation response of SMAs as shown experimentally in [133, 148], and in turn to the fracture behavior of these materials.

In contrast to most conventional structural materials, SMAs' fracture may be also thermo-mechanically assisted. According to recent experimental investigations [66, 60], SMAs may fracture during cooling under a constant external mechanical loading; this loading path is an idealization of typical loading paths that utilize these alloys

as actuators.

2.3.7 Nominal isothermal loading conditions

According to experimental results under nominal isothermal quasi-static loading [58], the fracture toughness dependence on temperature is piece-wise constant, below and above M_d (for nominal temperatures above M_d the austenite phase is stable and the deformation response of the SMA is similar to that of a conventional metal, with plastic deformation (via slip) occurring when the stress reaches the yield stress of austenite), with the fracture toughness above M_d, *i.e.*, the fracture toughness of austenite, being considerably higher. At temperatures below M_d, the extrapolated $K_{J_{I_C}}$-values, calculated using $K_{J_{I_C}} = \sqrt{E' \; J_{I_C}}$, where E' corresponds to the stable phase at the temperature at which the experiments were conducted, are representative of the fracture toughness of martensite. At those temperatures, the crack grows into a region of oriented martensite although the far-field material phase may be different, *i.e.*, self-accommodated martensite at temperatures at which martensite is stable or austenite in the pseudoelastic temperature range. The difference in the apparent elastic properties of the far-field material is an additional source of variability in the measured J_{I_C}-values at different temperatures below M_d that does not affect the extrapolated $K_{J_{I_C}}$-values.

It should further be noted that in the literature [161, 54, 140, 108], it was argued, based on LEFM, that the fracture toughness of SMAs depends monotonically on temperature. However, the published data, as discussed in [14], appears to be determined from tests that do not comply with the small-scale transformation condition which is a perquisite for LEFM to be valid.

2.3.8 Actuation loading conditions

The experimentally observed fracture of SMA specimens during phase transformation induced by cooling under a a constant external mechanical loading [66, 60], which from an energetic point of view may seem in disagreement with the general view of dissipative processes resulting in an enhancement of fracture toughness, is characteristic of SMAs and should be attributed to phase transformation from austenite to martensite interacting with the stress and strain fields near the notches/cracks. As explained on the basis of finite element simulations and analytical arguments [20], the increase of driving force for crack growth during cooling is due to transformation occurring in regions in front of the crack tip. Furthermore, stable crack growth was observed experimentally and this toughening response is shown to be mainly associated with the shielding effect of the transformed material left in the wake of the advancing crack [70].

No attempts to measure the fracture toughness of SMAs under actuation loading conditions have yet been reported.

3 Reversibility of transformation-induced fracture toughness enhancement.

As mentioned in previous chapter SMAs tend to show a stable crack growth which is clearly visible in resistance curves which are rising instead of being flat. Similar behaviour is observed in ductile elastic-plastic materials, which is due to their propensity to undergo irreversible deformation display an increasing resistance to progressive crack advance, *i.e.*, stable crack growth. A one-parameter description of stable crack growth by a fracture toughness vs crack advance (resistance) curve is possible under specific conditions. Here, experimental observations are reported to (i) demonstrate that the toughness enhancement due to crack advance in hysteretic materials may be "reversed" by partial unloading, which has implications on the evaluation of the resistance curve and its validity conditions, and (ii) provide an experimental verification of the theoretical insight into the mechanics of stable crack growth.

3.1 Introduction to reverse phase transformation in the wake of growing crack

In most dissipative material systems, cracks initially grow stably under increasing load until critical conditions are met. Such material systems are characterized by rising crack extension resistance curves, the so-called R-curves [183]. The R-curve slope is indicative of the relative crack growth stability and, thus, the entire R-curve provides a more complete description of the fracture response than a single fracture toughness value.

A simplistic rationale to stable crack growth is offered by the "energetic" argument that in order to maintain crack growth, energy must be supplied into the system to compensate for the work expended into the dissipative processes that accompany

crack advance. In conventional ductile materials, the consensus is that crack growth is stabilized by irreversibility effects associated with nonproportional straining in the active plastic zone and the irrecoverable deformation left in the wake of the growing crack [64, 136, 36, 137, 34]. It has been argued that (i) plastically deformed solids offer more resistance to nonproportional loading, which corresponds to advancing cracks, than to (nearly) proportional loading, which corresponds to stationary cracks, and, therefore, the strain at given distances from the crack tip are generally larger in stationary problems than in crack growth problems for the same crack configuration and load under small-scale yielding conditions; thus, it is necessary to continue to deform the material in order to maintain a suitably concentrated strain field at the advancing crack tip, and (ii) there is a fan ahead of the crack tip such that residual plastic deformation behind that fan and at sufficiently small distances from the crack tip impedes crack growth. The construction of the R-curve for such materials is based on concepts of elastic-plastic fracture mechanics, employing the J-integral as the fracture criterion [4]. The J-integral is based on nonlinear elasticity and inadequately models nonproportional inelastic deformation. However, under J-controlled crack growth conditions [63], which require nearly proportional inelastic deformation everywhere but in a small neighborhood of the crack tip, the J-integral can still be used to analyze crack growth.

Similar to ductile metals, phase transforming materials display stable crack growth under increasing load, known as transformation toughening [132, 92, 113, 24, 42, 110, 114, 91, 139, 80, 86, 53, 58]. In reversible phase transforming materials, reversibility of phase transformation and reorientation of martensite variants render the phenomenon of stable crack growth even more complicated than that in most ductile metals. These materials may fail by a combination of ductile tearing and cleavage, *e.g.*, NiTi and other SMAs [51, 122], and it is not yet clear what is the effect of reorientation on

the singularity of the strain fields close to the crack tip or whether the reversibility of phase transformation promotes or impedes crack advance [154, 17].

The present study offers the first experimental investigation of the effect of the reversibility of inelastic deformation on the apparent fracture toughness of advancing cracks and its implications in measuring resistance curves. NiTi compact tension specimen are tested under isothermal mechanical loading at a temperature at which phase transformation is reversible (superelastic loading). The loading paths include unloading to induce reverse phase transformation beyond that occurring during crack advance. The experimental observations in this study offer evidence that (i) partial unloading during stable crack growth may have a substantial impact on the fracture response, (ii) the compliance method for constructing the R-curve should be used with caution, and (iii) the validity conditions of R-curves are more strict in hysteretic materials than in conventional structural metals and, thus, the R-curve as a means to study the stability of a real structure is even less effective.

3.1.1 Dogbone testing and DSC for material characterization

A binary $Ni_{55.7}Ti_{44.3}$ (wt%) (Fig. 19), superelastic at room temperature, with phase transition temperatures $M_f = -29°C$, $M_s = -20°C$, $A_s = -15°C$ and $A_f = 7°C$, where M_f, M_s, A_s and A_f indicate martensite finish, martensite start, austenite start and austenite finish temperatures, respectively, was acquired from `Fort Wayne Metals`. The fracture tests are performed on compact tension specimens (schematic in Fig. 20a) at room temperature in an `MTS-810` servo-hydraulic test frame. The dimensions of the specimen are $W = 32.5$, $B = 8.5$, $0.45 \leq a/W \leq 0.55$, all in mm. The specimens are fatigue pre-cracked in load control with load values between 0 and P_{max} at a frequency of 10 Hz, where P_{max}, initially set equal to 20% of the highest load value expected in the subsequent fracture experiment, and was gradually decreased.

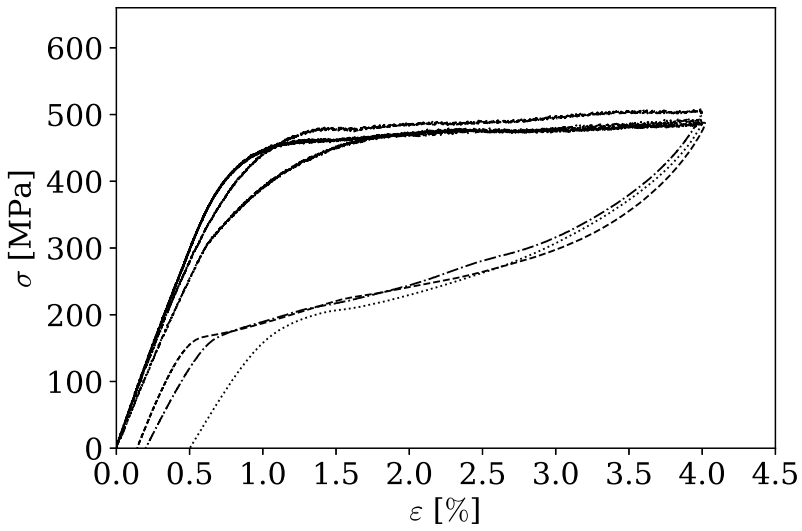

Figure 19: Uniaxial tensile loading–unloading stress–strain curves for 3 experiments performed on $Ni_{55.7}Ti$ (wt%) at room temperature.

The pre-cracked specimens are loaded in displacement control at a loading rate of 0.09 mm/min. Load and load line displacement using a clip on crack tip opening displacement extensometer by `Epsilon Technology Corp` are measured continuously at a rate of 10 Hz throughout the test. Optical images are recorded at a rate of 2 fps from one side of the CT specimens, which is speckled to produce a random pattern, using a `Point Grey Blackfly` CCD cameras equipped with `Canon 18-55mm` lens at an optical resolution of 0.02 mm/pixel. The optical images are post-processed via `Vic2D-6` software (developed by `Correlated Solutions`) to measure the full-field Lagrangian strain using Digital Image Correlation (DIC) [145].

3.1.2 Experiments to check master curve deviation

Load–load line displacement curves from the superelastic NiTi CT specimens that are unloaded/reloaded once are presented in Fig. 20(a and b). In both cases, the

material response is initially linear, followed by a nonlinearity associated with inelastic deformation: martensitic transformation, reorientation of martensite variants during crack advance, and possibly plastic deformation. During unloading back to 50% of the load, the behavior is again first linear followed by a nonlinear regime that is attributed to reverse phase transformation. Subsequent reloading displays a behavior similar to that of the initial loading with the load–load line displacement curves reaching eventually a peak value before descending to failure. A critical difference between the observed response and the respective one of conventional ductile metals and SMAs that do not display reverse phase transformation upon unloading (non-superelastic) (Fig. 24(c and d)) is the absence of a master curve, *i.e.*, the load-displacement curve after the unloading/reloading cycle does not return to the point at which unloading took place. This response should be attributed to (i) the recovery of the phase transformation strains left in the wake of the growing crack that are not fully restored during reloading, and (ii) the different direction and magnitude of the martensite variants formed upon reloading in the active transformation zone.

3.1.3 DIC results to confirm above mentioned phenomenon

DIC results depicting the surface strains close to the crack tip are presented in Fig. 21 at the instances denoted with a circle in Fig. 20b. Point 1 corresponds to the instant of unloading and point 2 to the instant at which the crack starts growing again upon reloading. According to these results, there is marked difference on the strain field that results in crack advance once sufficient unloading has taken place. The straining corresponding to point 2 in the load–load line displacement curve is in general lower than that corresponding to point 1 at given distances from the crack tip and there is straining in the wake of the growing crack that is not fully recovered upon reloading. Moreover, the strain field is not as symmetric and smooth at point 2 as is at point 1

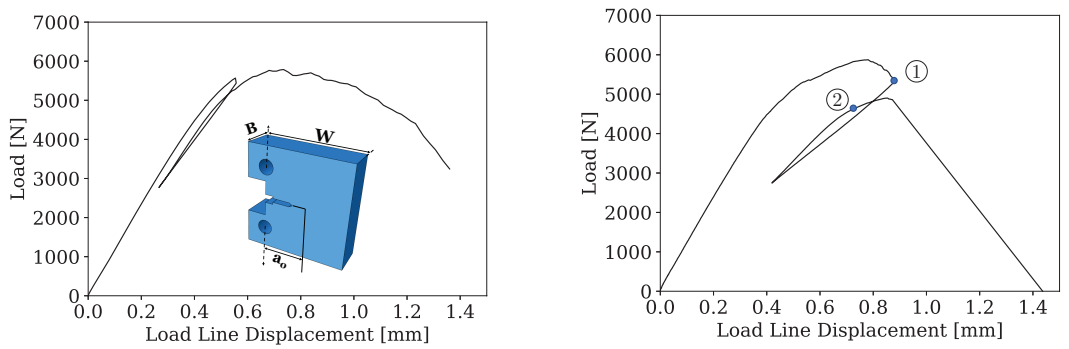

(a) and (b)

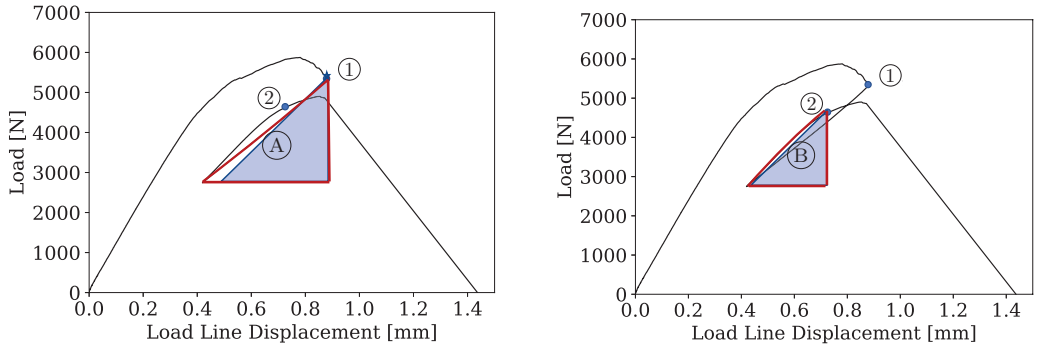

(c) and (d)

Figure 20: (a) and (b) shows experimental load–load-line displacement curves for CT specimen of superelastic $Ni_{55.7}Ti_{44.3}$ (wt%) (Fig. 19), (c) and (d) shows the regions A and B under the load-load line displacement are used for calculating the difference in the J-values between points 1 and 2.

(note the isocurve lines). As pointed out above, the aforementioned differences may also originate from the different direction and magnitude of the martensite variants formed upon reloading due to (i) changes in the loading direction in regions where re-orientation took place during crack advance before unloading, (ii) cyclic effects in the transformation response, and (iii) local stress redistribution due plastic deformation.

3.1.4 Conclusive evidence from above mentioned results

The resulted drop in the J-value required for crack advance due to unloading, *i.e.*, the difference, $J_1 - J_2$, between the J-values at points 1 and 2, is calculated using the

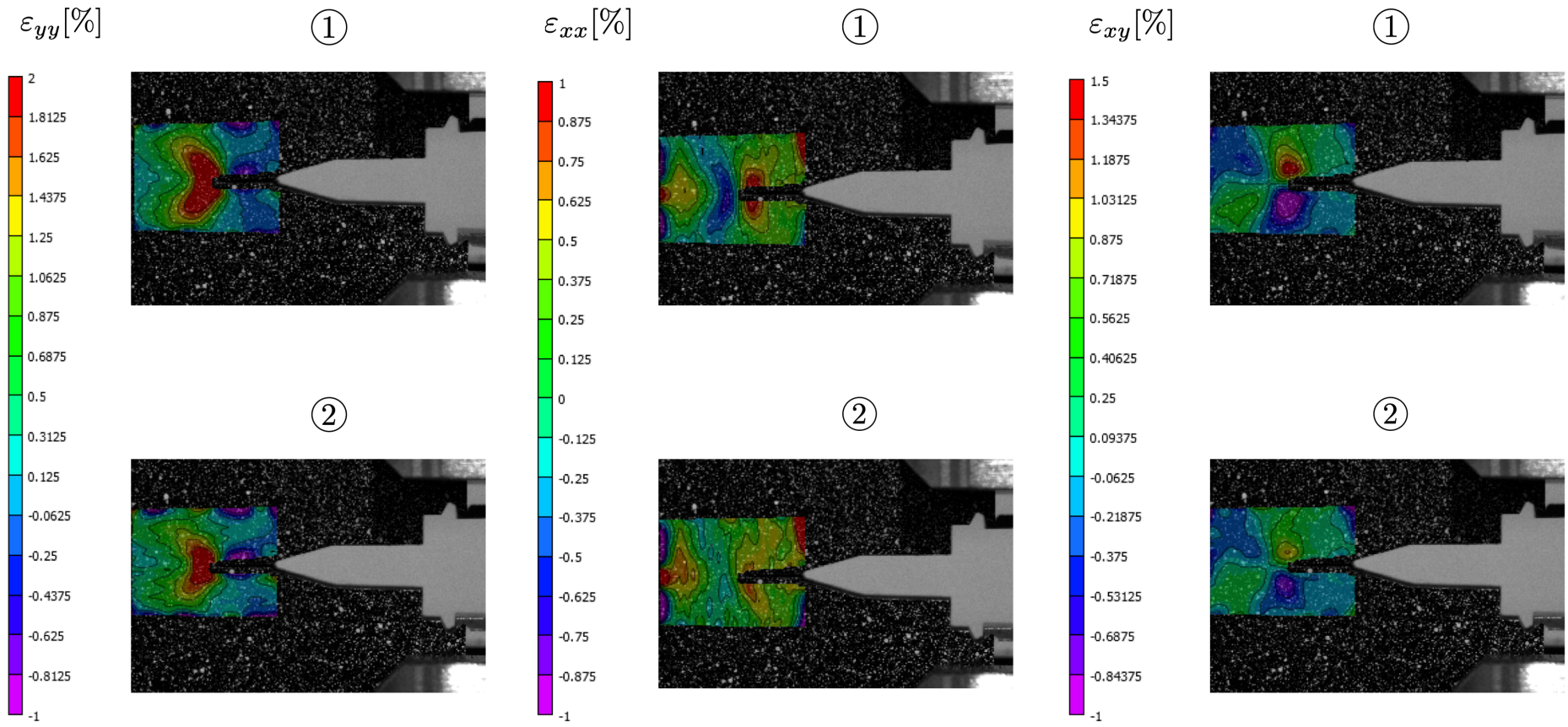

Figure 21: Surface strain contour plots obtained from *in situ* DIC referring to points 1 and 2 in Fig. 20b. The y-axis is in the direction of loading.

methodology developed [58] that relies on the ASTM E1820 [4] standard developed for conventional ductile materials. This methodology accounts for the change in the elastic properties induced by phase transformation, which, nevertheless, was shown to have a minor impact on the fracture toughness [101]. $J_1 - J_2$ is calculated from the load–load line displacement record by replacing the portion underneath the curve, area A (Fig. 20d), with area B, in the following equation, which approximates the J-value,

$$J = J^{el} + J^{in} = \frac{\eta^{el} A^{el}}{Bb} + \frac{\eta^{in} A^{in}}{Bb}, \tag{10}$$

A^{el} and A^{in} are the elastic and inelastic components of the area under the load–displacement curve, respectively, $b = W - a$ is the length of the unbroken ligament, and η^{el} and η^{in} are geometry-dependent factors [58, 101]. Namely,

$$J_1 - J_2 := -\left(J_A^{el} + J_A^{in}\right) + \left(J_B^{el} + J_B^{in}\right)$$

$$= -\left(\frac{\eta^{el} A_A^{el}}{Bb} + \frac{\eta^{in} A_A^{in}}{Bb}\right) + \left(\frac{\eta^{el} A_B^{el}}{Bb} + \frac{\eta^{in} A_B^{in}}{Bb}\right) \approx 7 \text{ KJ/m}^2, \tag{11}$$

where A_A^{el} and A_A^{in} determine the elastic and inelastic components of the energy released upon unloading (region A), respectively, and A_B^{el} and A_B^{in} determine the corresponding components of the energy stored upon reloading (region B) (Fig. 20d). The crack length needed for evaluating b is measured by the evolution of the elastic compliance [78, 4]. The level of decrease of the "apparent" toughness value is roughly 8% of the J_1-value, $J_1 \approx 88$ KJ/m^2; in general, it is dependent on the extend of unloading, *i.e.*, the extend of recovery of the phase transformation strains. It should be noted that the value $J_1 \approx 88$ KJ/m^2 is approximated by equation (10), which holds for static cracks. For advancing cracks, equation (10) should be corrected [4]. According to the ASTM standards, such a correction requires multiple unloading/reloading

cycles. A similar analysis yields that the drop in the "apparent" fracture toughness due to the unloading–reloading cycle in the experiment of Fig. 20a is approximately 2 KJ/m^2.

3.2 Experiments performed pertaining to ASTM standards

Further experiments were performed with multiple unloading/reloading cycles as recommended by the ASTM standards for measuring R-curves. From the unloading/reloading cycles, the elastic compliance is measured, which is needed for distinguishing between the elastic and inelastic components in the ASTM recommended incremental correction of (10) for advancing cracks [4] (Fig. 23(a and b))

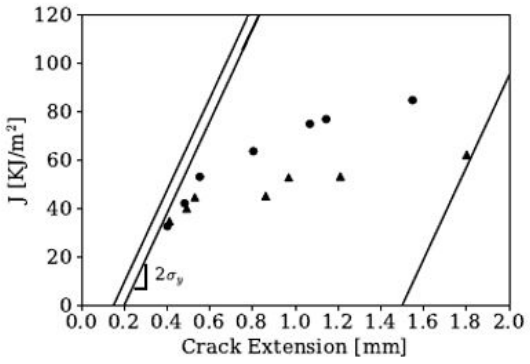

Figure 22: Represent the construction lines, *i.e.*, the exclusion lines and the 0.2mm offset line, needed for the experimental measurement of the R-curve according to the ASTM standards [4].

In these experiments, the unloading is smaller than 50% of the load at the instant of unloading, which is the unloading performed in the experiments presented thus far and corresponds to the maximum value permitted in the ASTM standards. Moreover, for comparison purposes, load–load line displacement curves from experiments performed on solution heat-treated NiTi CT specimen are shown in Fig. 24(a and b). The material in these experiments is prone to plastic deformation and non-superelastic.

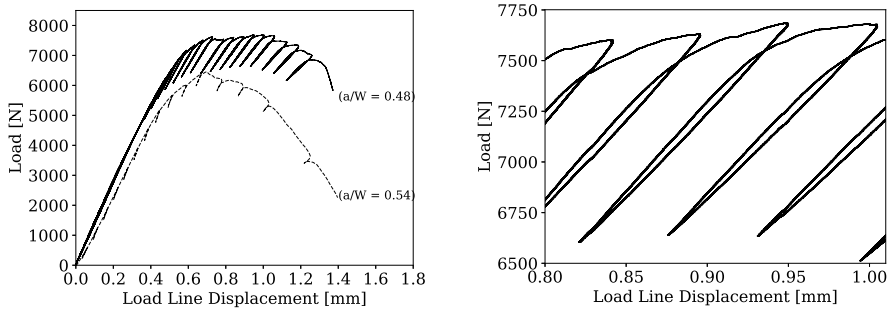

(a) and (b)

Figure 23: A magnified view of the curve depicted by the solid line in Fig. 23a Experimental load–load line displacement curves for NiTi CT specimens with multiple unloading/reloading cycles.

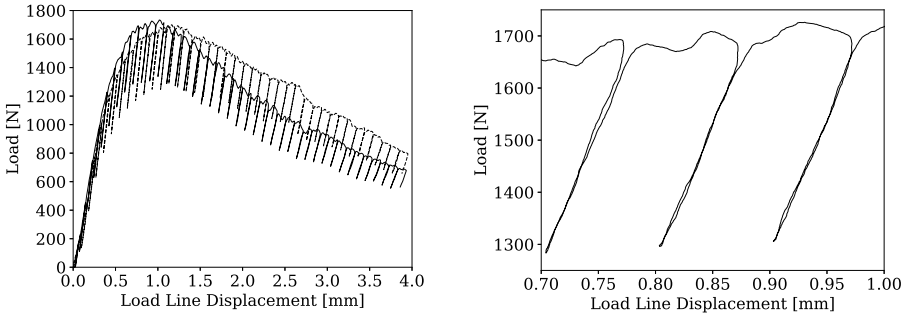

(a) and (b)

Figure 24: A magnified view of the curve depicted by the solid line in Fig. 24a, Non-superelastic (solution heat-treated) NiTi [58]. The unloading is just a fraction of the maximum allowed in ASTM E1820 [4] standards, *i.e.*, 50% of the load at the instant of unloading.

A magnified view of the experimental curves shows that the material response of the superelastic NiTi during the unloading/reloading cycle is still nonlinear (Fig. 23b) in contrast to the respective response of the non-superelastic NiTi (Fig. 24b) and the conventional ductile metals. The deviation from linearity is not as pronounced as it was in the experiments presented in Fig. 20 due to the smaller recovery of the transformation strains by the lower extend of unloading. Therefore, the resulted change in the J-value needed for crack advance due to an unloading/reloading cycle is not as drastic as that in the previous experiments. However, the cumulative effect of

multiple unloading/reloading cycles may still have a substantial impact on both the load–load line displacement curve (Fig. 23a) and the resistance curve (Fig. 22). Thus, the extent of unloading, which in one experiment (solid line) is triple that in the other (dashed line) should be responsible, together with material variability, for the pronounced discrepancy in the R-curves obtained from the two experiments (Fig. 22) using the methodology detailed in [101].

4 Experimental fracture toughness measurements under actuation loading conditions.

Experimental measurements of the fracture resistance of SMAs under thermomechanical loading conditions are reported in above chapters and new findings have been reported, which shows experimental evidence of anti-shielding effect due to reverse phase transformation in the wake of growing crack. It also shows possible issues that can be caused during fracture toughness experiments while using compliance method for crack growth. There is a certain need for isobaric fracture toughness experiments to see if stable crack growth in SMAs can be observed during thermal loading. NiTi compact tension specimens are subjected to either isothermal mechanical or isobaric thermal loading; the latter loading path is an idealization of typical loading paths that utilize these alloys as actuators. In this chapter a single-parameter description of the experimental data is employed on the basis of a path-independent contour integral, which is approximated by the load–load-line displacement curves recorded from the experiments. The obtained results represent the first experimental measurement of the fracture toughness of SMAs under coupled thermo-mechanical loading, and indicate that the fracture toughness enhancement associated with crack advance under isobaric thermal loading is less pronounced than the corresponding one under isothermal mechanical loading.

4.1 Fracture resistance under thermomechanical loading

Resistance to fracture, measured as a configuration-independent resistance curve (R-curve) or as a critical point, plays a crucial role in material assessment/ranking, damage-tolerant design, and structural integrity evaluation.

SMAs are intermetallics, a relatively brittle class of materials, which fail predominantly by cleavage of specific crystallographic planes [14, 142, 54, 160, 103]. However, SMAs do display slow and stable crack extension, *i.e.*, an R-curve behavior, which is attributed mainly to phase transformation as opposed to plastic deformation in conventional ductile metals. The observed toughening (stable crack growth) is due to irreversibility effects associated with nonproportional straining in the active phase transformation zone and the shielding effect of the transformed material left in the wake of the advancing crack. Stable crack advance has been observed under nominally-isothermal mechanical loading and during cooling under a constant applied load, *i.e.*, under thermomechanical (also termed actuation) loading [75]. Crack advance under the latter loading conditions, which is characteristic to SMAs, is argued to initiate due to transformation occurring in regions in front of the crack tip, resulting in an increase of the crack driving force [20, 70].

Phase transformation (and (re)orientation of martensite variants) occurring during the fracture of SMAs call for modifications to the experimental measurement of fracture toughness standards developed for conventional structural metals [4]. Recently [58], proposed a measurement of the J_R-resistance curve under nominally-isothermal mechanical loading that accounts for the mismatch among the apparent elastic properties of austenite, self-accommodated, and oriented martensite. Further modifications to the ASTM standards regarding the linear compliance method, blunting line slope, and the thickness requirement for J-dominance may be required for the standardization of fracture toughness testing for SMAs as discussed in [102].

In this technical note, a path-independent contour integral is employed for describing the driving force for crack growth in SMAs under thermomechanical (actuation) loading paths, which collapses to the J-integral under nominally-isothermal conditions. An approximation of this integral is measured experimentally from the

load–load-line displacement curve recorded from experiments on NiTi Compact Tension (CT) specimen during cooling under a constant bias load. The measured R-curves are presented and compared with those obtained from the same material under nominally-isothermal conditions. The obtained results represent the first experimental measurement of the fracture toughness of SMAs under actuation loading and support the introduction of the employed contour integral as a potential unified descriptor of fracture toughness in SMAs for a wide range of thermomechanical loading conditions (and geometric configurations). confirm that the point fracture toughness of martensite is temperature-independent.

4.2 Path-independent contour integral during isobaric actuation

For introducing a path-independent contour integral that can achieve similitude over a wide range of loading conditions and geometric configurations, the SMA deformation response is approximated by a thermo-hyperelastic material law with a Helmholtz free energy of the form

$$\psi(\varepsilon_{ij}, T) \equiv u\left[\varepsilon_{ij}, s(\varepsilon_{ij}, T)\right] - Ts(\varepsilon_{ij}, T), \tag{12}$$

where u is the specific internal energy, $s = -\frac{\partial \psi}{\partial T}$ is the specific entropy, $T = \frac{\partial u}{\partial s}$ is the absolute temperature, and ε_{ij} are the components of the small strain tensor.

Assuming quasi-static loading, the energy release at the crack tip per unit crack extension, 2γ, is given from global energy considerations as [111, 2]

$$2\gamma\dot{a} + \frac{dU}{dt} = \frac{dW_{ext}}{dt} + \frac{dH}{dt}, \tag{13}$$

where Π is the potential energy of the system, U is the internal energy, W_{ext} is the

external work done, H is the heat input, and $\dot{a} > 0$ is the crack velocity. Assuming plane strain conditions, ignoring body forces and heat sources/sinks, and taking into account the Legendre transformation (12) and the definition of the small strain tensor, the above energy balance can be written

$$2\gamma\dot{a} + \frac{d}{dt}\left(\int_\Omega \rho\psi \, dV\right) = \int_\Gamma n_i \sigma_{ij} \frac{\partial u_j}{\partial t} \, dS - \frac{d}{dt}\left(\int_\Omega \rho T s \, dV\right) - \int_\Gamma q_i n_i \, dS, \tag{14}$$

where Ω is the cracked configuration, bounded by contour Γ, ρ is the density, σ_{ij} are the components of the stress tensor, q_i are the components of the heat flux vector, n_i those of the unit vector normal to the Γ, and u_i are the components of the displacement vector. Assuming that the displacement and temperature distributions move rigidly with the crack tip in the region Ω, the temperature is bounded at the crack tip, and the crack grows in the x_1-direction, the following relations hold true [111]

$$\frac{\partial u_j}{\partial t} = -\dot{a}\frac{\partial u_j}{\partial x_1}, \quad \frac{\partial T_j}{\partial t} = -\dot{a}\frac{\partial T_j}{\partial x_1}, \quad \frac{d}{dt}\left(\int_\Omega \rho\psi \, dV\right) = -\dot{a}\int_\Gamma n_i \rho\psi \, dS, \tag{15}$$

$$\int_\Gamma q_i n_i \, dS = \int_\Omega \frac{\partial q_i}{\partial x_i} \, dV = \int_\Omega \rho s \frac{\partial T}{\partial t} dV - \frac{d}{dt}\left(\int_\Omega \rho T s \, dV\right). \tag{16}$$

For the derivation of the last equation,

$$\frac{dU}{dt} = \frac{dW}{dt} + \frac{dH}{dt}, \tag{17}$$

which holds for every thermomechanical process, and (12) were taken into account, where $W = \int_0^{\varepsilon_{ij}} \sigma(\varepsilon_{ij}, T) d\varepsilon_{ij}$ is density of total stress work. Given (15) and (16), the energy balance equation (14) takes the form

$$J^* = \int_\Gamma \left(\psi dx_2 - \sigma_{ij}\frac{\partial u_j}{\partial x_1} ds\right) + \int_\Omega s\frac{\partial T}{\partial x_1} dA = 2\gamma. \tag{18}$$

To prove the path-independence of J^*, it suffices to show that $J^* \equiv 0$ when integrated over any defect-free region Ω^*, bounded by contour Γ^*. To this end, note that the differential of the equation of state (12) asserts that

$$\frac{\partial \psi}{\partial x_k} = \frac{1}{\rho}\sigma_{ij}\frac{\partial}{\partial x_i}\left(\frac{\partial u_j}{\partial x_k}\right) - s\frac{\partial T}{\partial x_k} \overset{\frac{\partial \sigma_{ij}}{\partial x_i}=0}{\Rightarrow} \frac{\partial}{\partial x_i}\left(\rho\psi\delta_{ik} - \sigma_{ij}\frac{\partial u_j}{\partial x_k}\right) + \rho s\frac{\partial T}{\partial x_k} = 0. \quad (19)$$

Assuming plane strain conditions, integration of the above equation results in

$$\int_{\Gamma^*} n_i\left(\psi\delta_{ik} - \sigma_{ij}\frac{\partial u_j}{\partial x_k}\right)ds + \int_{\Omega^*} s\frac{\partial T}{\partial x_k}dA = 0, \quad (20)$$

and, thus, for $k = 1$, $J^* = 0$.

4.3 Uniaxial test and DSC for material characterization

Fracture toughness tests are performed on $Ni_{55.7}Ti_{44.3}$ (wt%) Compact Tension (CT) specimens. The phase transition temperatures of the alloy, which is superelastic at room temperature (Fig. 25), are $M_f = -29°C$, $M_s = -20°C$, $A_s = -15°C$ and $A_f = 7°C$, where M_f, M_s, A_s and A_f indicate martensite finish, martensite start, austenite start and austenite finish temperatures, respectively, determined from Differential Scanning Calorimetry (DSC).

The isothermal tests are performed in displacement control at a loading rate of 0.09 mm/min. The isobaric fracture tests are conducted by inductively heating the CT specimen to 100°C to ensure complete transformation to austenite, increasing the load to one that corresponds to 95% of isothermal K_{I_C} to ensure small-scale transformation conditions at initiation of crack growth, and then cooling down at a rate of 1°C /min to room temperature. Crack extension is measured by the elastic compliance method [29, 78], in accordance with the ASTM standards [4]. Optical images are recorded on one side of the CT specimens to measure the full-field Lagrangian strain

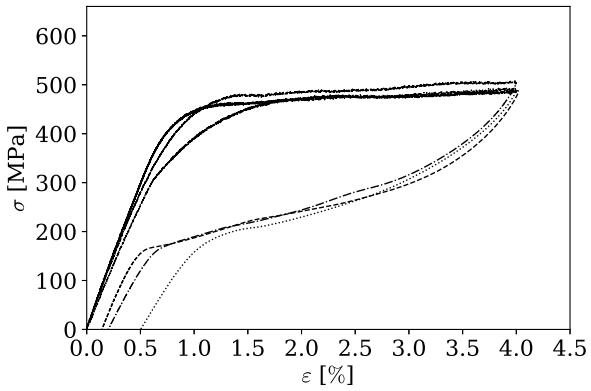

Figure 25: Uniaxial tensile loading–unloading stress–strain curves for 3 experiments performed on $Ni_{55.7}Ti$ (wt%) at room temperature.

using Digital Image Correlation (DIC). For further details on the experiments, please, see the supplementary material provided.

4.4 Comparing isobaric and isothermal experiments

The experimental load-load-line displacement curves are shown in Figures 26. In the isothermal tests, the response is initially linear, characterized almost entirely by elastic deformation, followed by a nonlinearity associated with increasing phase transformation close to the crack tip, crack advance and resulting reorientation of martensite variants, and to a lesser extent plastic deformation [160], before final failure. The monotonicity of the applied load is interrupted by a sequence of partial unloading/reloading cycles performed in order to measure the CT specimen compliance and in turn the crack advance. The load-load-line displacement curves for the isobaric experiments are mostly linear during the application of the mechanical load at 100°C. During the subsequent cooling while the bias load is kept constant, the load-line displacement increases as the phase transformation zone expands close to

the crack tip, where the stresses are high, due to the Clapeyron slope, interrupted periodically by partial unloads/reloads. Reorientation of martensite variants is expected in the wake of the growing crack.

The experimental measurement of the path-independent contour integral J^*, introduced in section 4.2, can be based on its energetic definition

$$J^* = -\frac{d}{da}\left(\int_\Omega W\, dV + \int_\Gamma n_i \sigma_{ij} u_j\, dS\right), \tag{21}$$

derived from (13) and (17). Under the assumption of fixed displacements (grips), the second term in the above equation vanishes, and J^* can be approximated as

$$J^* \approx \int_0^\delta \left(\frac{\partial P}{\partial a}\right)_\delta d\delta, \tag{22}$$

where P is the imposed force per unit thickness and δ is the load point displacement [135].

The J^*-value can therefore be measured from the load–load-line displacement record of a CT specimen by correlating J^* and the work of deformation $\int_0^\delta P d\delta$, *i.e.*, the area under the load–displacement curve [40, 116, 30], as $J^* = J^{*^{el}} + J^{*^{in}} = \frac{\eta^{el} A^{el}}{Bb} + \frac{\eta^{in} A^{in}}{Bb}$, where B is the specimen thickness, $b = W - a$ is the length of the unbroken ligament (W is the specimen width and a the crack size). A^{el} and A^{in} are the elastic and inelastic components of the area under the load–load-line displacement curve, respectively. η^{el} and η^{in} are geometry-dependent factors, the existence of which is discussed in [58, 102]. The expression for the J-integral given above is valid only for constant crack length, a. For advancing cracks, an incremental formulation is needed [41], $J_i^* = J_i^{*^{el}} + J_i^{*^{in}}$, where $J_i^{*^{el}}$ and $J_i^{*^{in}}$ are evaluated from the previous step $J_i^\alpha = \left[J_{i-1}^\alpha + \frac{\eta_{i-1}^\alpha}{Bb_{i-1}} A_{i-1,i}^\alpha\right]\left[1 - \frac{\gamma_{i-1}^\alpha}{b_{i-1}}(a_i - a_{i-1})\right]$. In the last equation, the superscript $^\alpha$ stands for either ^{el} or ^{in}, $A_{i-1,i}^{el}$ and $A_{i-1,i}^{in}$ are the increments of the elastic and inelastic

areas under the load–load-line displacement record from step $i-1$ to i, respectively, $A^{\alpha}_{i-1,i} = \frac{1}{2}(P_i + P_{i-1})(\delta^{\alpha}_i - \delta^{\alpha}_{i-1})$, where $\delta^{el}_i = P_i C_i$ and $\delta^{in}_i = \delta_i - \delta^{el}_i$ are the elastic and inelastic components of the displacement, and C_i is the unloading elastic compliance. γ^{el} and γ^{in} are geometry-dependent factors and can be determined using η^{el} and η^{in}, respectively [58, 102].

Table 1: J_{I_C}-values [KJ/m^2] for $Ni_{55.7}Ti_{44.3}$ (wt%) SMA determined by the method of offset line from isothermal and isobaric fracture experiments with unloading–reloading steps to determine the system compliance.

	Isothermal		Isobaric	
Experiment	A	B	C	D
J_{I_C}-value [KJ/m^2]	31.9	30.3	27.8	24.6

Once J^* and Δa values are known, as outlined above and detailed in [58, 102], the J^*_R-curves are constructed according to the ASTM standards (Fig. 26). A construction line is plotted from the origin of J^* vs Δa plot with a slope of $2\sigma_Y$, where σ_Y is the effective yield strength, *i.e.*, the average of the critical stress, σ_{cr}, required for initiation of phase transformation and the ultimate tensile strength, σ_{TS}. The J^*-Δa data points that fall between two exclusion lines, which are drawn parallel to the construction line intersecting the abscissa at 0.15 mm and 1.5 mm, are plotted and a power-law regression is fit throughout. To determine the $J^*_{I_C}$ fracture toughness, an offset line is then plotted parallel to the construction line, intersecting the abscissa at 0.2 mm. The intersection of the 0.2 mm offset line and the regression line defines an interim value of the J-integral. This interim value is considered a conservative, constraint-independent fracture toughness value if the qualification requirement of ASTM standards [4], $B > 10\ J^*_{I_C}/\sigma_Y$, related to the specimen thickness is met.

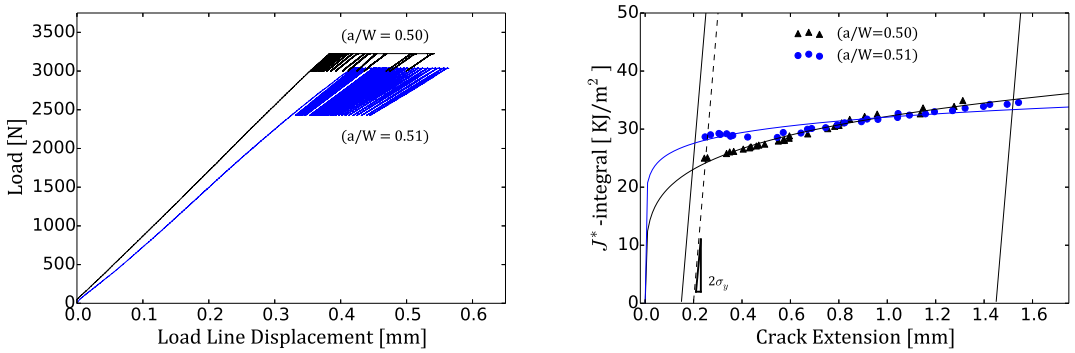

(a) and (b)

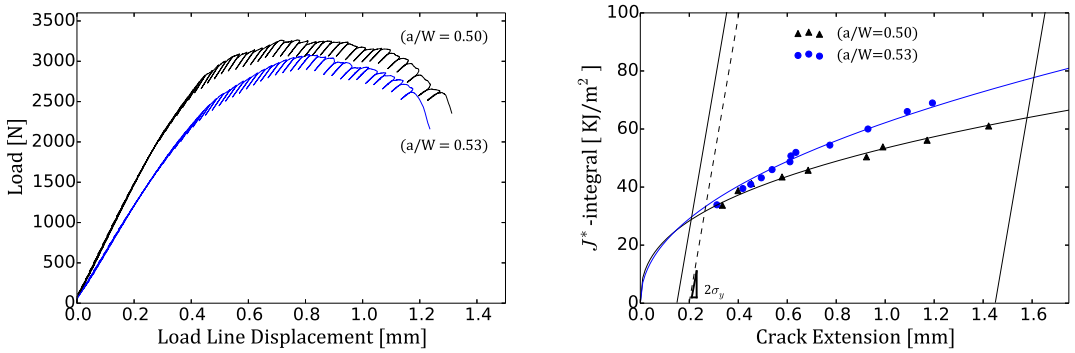

(c) and (d)

Figure 26: Load-Load-line displacement (LLD) and J_R^*-curves for the isobaric and isothermal fracture tests. In all experiments $0.45 < a/W < 0.55$, and $3.95 < B < 4.05$ mm. (a) & (b) isobaric experiments and (c) & (d) isothermal experiments.

4.5 Observations made from isobaric experiments and DIC results

- The critical $J_{I_C}^*$-values measured using the 0.2 mm offset approach from all experiments are close to each other (Table 1). The ∼10–15% difference among the critical values measured should be attributed to the following factors: (i) The quasi-brittle transgranular (quasi-cleavage) fracture and pronounced material variability in the deformation response of SMAs (Fig. 25) result in a

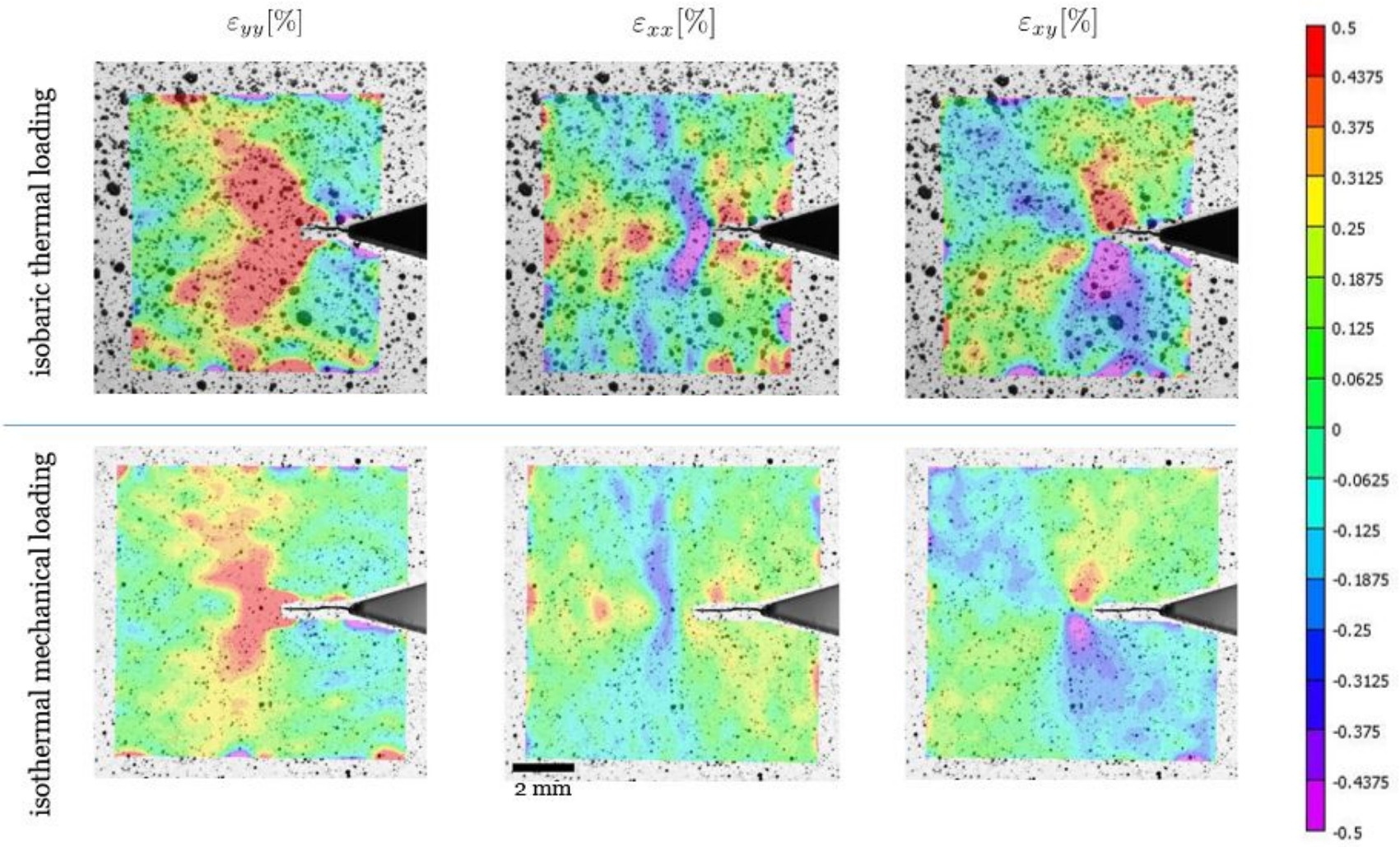

Figure 27: Surface strain contour plots obtained from *in situ* DIC on the $Ni_{55.7}Ti_{44.3}$ (wt%) CT specimens under two different thermomechanical loading paths. The y-axis is in the direction of loading. Note that the strain values at given distances from the crack tip are larger for the isobaric thermal loading although the crack length is smaller.

pronounced failure response variability; (ii) The default slope, $2\sigma_Y$, of the offset line approximates the apparent crack advance due to crack-tip blunting when there is no slow stable crack tearing. This approximation assumes that, before tearing, the crack advance is equal to one half of the crack-tip opening displacement under nominally-isothermal mechanical loading. However, crack-tip blunting in SMAs is path-dependent [11] and, thus, such a slope should assume different values for the two loading conditions (isothermal vs isobaric).

- The proximity of the critical values obtained corroborates that the path-independent J^*-integral can capture enough of the correct physics to describe with sufficient accuracy the driving force for crack advance in SMAs under both tested conditions. Due to the theoretical arguments resulting in its definition (further discussed below), the J^*-integral may be adopted as an engineering tool for fracture of SMAs under a wide range of thermomechanical loading conditions and crack configurations. purpleIt should be noted that the proximity in the J_{IC}-values is attained while the strain fields under isothermal mechanical loading are quite different than the corresponding ones during isobaric thermal loading; the spatial distribution of the strain fields is quite similar but the strain values that correspond to isobaric thermal loading at similar locations with respect to the crack tip are quite higher (Fig. 27). In the former case, the driving force for crack growth is the increasing load-line displacement, which results in stress-induced martensite close to the crack tip and bias load changes. In the latter case, the driving force is the thermomechanically-induced phase transformation which results in increasing load-line displacement while the bias load is kept constant.

- The slope of the isothermal J^*_R-curves is steeper than that of the isobaric ones, which indicates that the toughness enhancement associated with crack advance

under isothermal conditions is more pronounced than the corresponding one under isobaric conditions. The consensus is that the toughness enhancement associated with crack advance is attributed to irreversibility effects associated with nonproportional straining in the active inelastic zone and the irrecoverable deformation left in the wake of the growing crack [64, 136, 36, 137, 34, 104]. Unfortunately, it is not clear from the DIC results alone how these two stabilizing mechanisms are affected by the thermomechanical loading paths considered; numerical simulations may contribute towards the required insight.

Given its definition, the J^*-integral should be further applicable for thermomechanical loading paths for which the deformation response of SMAs can be approximated by a potential $\psi(\varepsilon_{ij}, T)$ such that for a given loading path there is an "1–1" correspondence between the stress $\sigma_{ij} = \rho\frac{\partial\psi}{\partial\varepsilon_{ij}}$ and strain ε_{ij}; such an approximation is expected to be valid for a wide range of thermomechanical loading paths involving nearly proportional mechanical loading and monotonic temperature changes.

5 On the fracture response of SMAs by void growth and coalescence

Previous chapters discussed in details the required changes in ASTM standards to calculate error free fracture toughness SMAs. Anti-shielding effect due to reverse phase transformation, doubts about compliance method for crack growth calculations, and also showed first ever evidence of stable crack growth for pseudoelastic SMAs under isobaric actuation. Now to address why crack tip blunting is not prominent is SMAs and why SMAs tend to fail in a quasi-cleavage manner rather that cleavage alone which is observed in other intermetallics. Its important to study the impact of phase transformation on void growth and coalescence, which will be done in this chapter.

5.1 Void formation/growth/coalescence impacting SMAs failure properties

SMAs are intermetallics with unique properties stemming from a reversible diffussionless solid to solid phase transformation from austenite to martensite [117, 125, 119, 89, 7, 69]. Phase transformation may result in large deformations and generation/absorption of heat that impact the fracture response of SMAs along with the reversibility of phase transformation, (re)orientation of martensite variants, overload and TRIP [162, 99, 141, 32, 33, 31, 53, 143, 13]. Despite belonging to a relatively brittle class of materials, that of intermetallics, the fracture response of SMAs is characterized by cleavage of specific crystallographic planes with a strong presence of dimples that are indicative of ductile rupture [49, 53, 122]. Ductile rupture involves in general nucleation, growth, and coalescence of microvoids.

The existing literature on the fracture response of SMAs deals almost entirely

with *extrinsic* shielding resulting from inelastic deformation left in the wake of the crack. Analytical and numerical analyses of the mechanical fields close to the crack tip [176, 178, 165, 167, 107, 105, 12, 10, 126], of the levels of fracture toughness enhancement as a function of transformation metrics [154, 46, 19, 17], and of the role of transformation-induced contraction [174], latent heat effects [15, 180], and reversibility of phase transformation [154, 17, 61, 77] in the fracture resistance of SMAs have been reported in literature. Recently, it has been observed that large-scale phase transformation resulting from temperature changes, *i.e.*, cooling, may also promote crack advance [18, 66, 72, 73]. These numerical investigations are based on either (i) LFEM tools, assuming that the mechanical fields in the near-tip region are dictated by a linear elastic response, such as the virtual crack closure technique [19, 18], (ii) on cohesive elements, which essentially couple a fracture process model to the stress and strain field of a growing crack [154, 46], or (iii) specialized finite element methods for steady state crack growth based on the path independence of the J-integral in such conditions [17, 15, 61]. These, so-called *"global"*, approaches do not pay attention to the failure micromechanisms and have been proven inadequate to describe the fracture of structural metals in many cases of complex loading conditions involving large-scale yielding, mixed-mode cracking, or non-isothermal loading, and for capturing size effects. By way of contrast, the *"local"* approaches to fracture aim at predicting the fracture toughness of specimens or the fracture load of components on micromechanistical grounds [93, 130, 131, 21].

Void formation/growth/coalescence and cleavage are in general *intrinsic* damage mechanisms promoting crack advance. In addition to phase transformation, the presence of precipitates in large volume fractions, which act as void initiation sites, is another clear differentiator of SMAs from other intermetallics. Ni-rich NiTi alloys are generally heat treated to produce metastable Ni_4Ti_3 precipitates, of large volume

fractions, which have been estimated around $2 \sim 7\%$ depending on aging [35]. Large second phases are also present in both Ti-rich ($NiTi_2/Ni_2Ti_4O_x$–type) and Ni-rich ($TiNi_3$-type) compositions. Decreasing Ni_4Ti_3 precipitate size results in a less "ductile" response and a weaker presence of dimples in the fracture surface of SMAs [49]. Similar is the effect of decreasing grain size [1]. Both have been attributed to a strengthening of the matrix against dislocation plasticity. In an effort to examine the role of stress triaxiality on the ductility of SMAs at fracture [122], performed experiments on notched round-bars. Similarly to ductile structural metals, the higher the triaxiality, the lower the fracture strain measured. However, in contrast to most ductile structural metals, no evidence of the characteristic cup-and-cone fracture surface or penny-shaped cracks on smooth or mildly notched specimens was observed. The fracture response, although ductile in terms of relatively large fracture strains, was characterized by cleavage with a strong presence of microvoids initiated from inclusions and precipitates.

Fractography, stress–strain, and R-curves alone cannot yield information on the relative importance of the fracture modes or any information about the material deformation response prior to failure. Thus, numerical simulations should be employed to assist experiments in gaining a further insight into the mechanisms that drive fracture in SMAs. [122] resorted to the Rice–Tracey void-growth model [138] to justify the experimental indications that macroscopic fracture initiation is stress-controlled and starts at the notch-root, *i.e.*, coalescence of voids results from cleavage fracture rather than plastic collapse of the intervoid ligament. Similarly. [5, 6], developed a constitutive model that accounts for void growth in the realm of the Gurson–Tvergaard–Needleman model [56, 157, 28], which assumes a stress-triaxiality dependence on the strain and void-volume fraction evolution in order to simulate experimental results.

Both the aforementioned models *a priori* assume that void growth has a strong influence on the fracture response of SMAs and that plastic deformation is the dominant mechanism contributing to void growth.

In contrast to the aforementioned studies, the objective of the present paper is to investigate void growth and coalescence in precipitation-hardened SMAs by unit cell simulations and, by comparison to the available experimental data, draw conclusions on their importance on the fracture response of these materials. Pioneered by Koplik and Needleman [83], numerical investigations of unit cells have been a useful tool to investigate void initiation, growth, and coalescence in the mesoscale [25, 81, 44, 146, 67]. The unit cell consists of a single void, assumed to have originated from a second phase particle. The constitutive response of the surrounding matrix includes phase transformation and plastic deformation. The deformation history prior to void nucleation and its potential effect on microstructure evolution are ignored, *i.e.*, no void nucleation is taken into account, and, thus, only void growth and coalescence are studied.

5.2 Problem formulation

5.2.1 Constitutive response

The constitutive law can describe the isothermal response of SMAs in a temperature range at which the initially stable austenite state fully transforms to martensite upon loading prior to deforming plastically at higher load levels (Figure 28). The isothermal assumption is valid for a range of strain rates within the regime of quasistatic processes. For higher loading rates, the generation of heat during phase transformation from austenite to martensite may result in strong thermomechanical coupling, which is not accounted for herein for simplicity [148, 39].

The constitutive law is based on the Eulerian logarithmic (Hencky) strain [62],

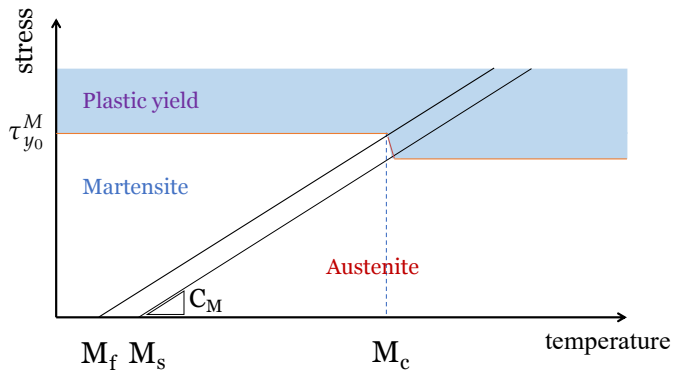

Figure 28: Stress–temperature phase diagram. The model can describe the isothermal response of SMAs in the temperature range $M_s < T < M_c$ at which the material, initially in the austenite state, fully transforms to martensite before deforming plastically at yield stress $\tau_{y_0}^M$.

its conjugate Kirchhoff stress, the objective logarithmic time rate [134, 171], and the additive decomposition of total stretching (or rate of deformation) into elastic, transformation, and plastic parts. The numerical implementation of the model is based on an *incrementally objective* algorithm in which the evolution equations of the tensorial state variables described below are mapped and integrated in a local configuration and subsequently the discrete equations are mapped back to the Eulerian description [150, 181]. The constitutive model and its numerical implementation have been verified and benchmarked in [172, 181].

5.2.2 Kinematics

The Hencky strain

$$h_{ij} = \frac{1}{2}\ln\left(b_{ij}\right) = \sum_{\alpha=1}^{m} \ln\left(\lambda^{\alpha} b_{ij}^{\alpha}\right), \tag{23}$$

is introduced as the logarithmic measure of the left Cauchy-Green deformation tensor with components b_{ij}, where λ^{α} are the m distinct eigenvalues of b_{ij}, b_{ij}^{α} are the components of the corresponding eigenvectors, and $i, j = 1, 2, 3$.

The objective logarithmic time rate of the Hencky strain

$$\mathring{h}_{ij} = \dot{h}_{ij} + h_{im}\Omega_{mj} - \Omega_{im}h_{mj} = D_{ij}, \tag{24}$$

yields the total stretching, D_{ij}, where $\Omega_{ij} = W_{ij} + \sum_{\alpha\neq\beta}^{n} \left(\frac{1+(\lambda^\alpha/\lambda^\beta)}{1-(\lambda^\alpha/\lambda^\beta)} + \frac{2}{\ln(\lambda^\alpha/\lambda^\beta)} \right) b^\alpha_{im} D_{mn} b^\beta_{nj}$, W_{ij} are the components of the spin tensor, and "$\dot{}$" denotes material time rate.

The logarithmic rotations, defined from the differential equation

$$\dot{R}_{ij} = \Omega_{im}R_{mj}, \quad R_{ij}|_{t=0} = \delta_{ij}, \tag{25}$$

define a locally rotating coordinate system in which the material time rates of the rotated (Langrangean) tensors are objective, *i.e.*,

$$R_{im}\dot{a_{mn}}R_{jn} = R_{im}\mathring{a}_{mn}R_{jn} \tag{26}$$

holds, where a_{ij} are the components of an arbitrary tensor.

Time integration of (26), assuming $a_{ij} = h_{ij}$ and $h_{ij}|_{t=0} = 0$ for all i and j, yields

$$h_{ij} = R_{mi}\left(\int_0^t R_{mk}\mathring{h}_{kl}R_{nl}\mathrm{d}t\right)R_{nj} \overset{(24)}{=} R_{mi}\left(\int_0^t R_{mk}D_{kl}R_{nl}\mathrm{d}t\right)R_{nj}, \tag{27}$$

and, thus, additive decomposition of D_{ij} into elastic, transformation, and plastic parts yields an additive decomposition of the Hencky strain

$$h_{ij} = h^e_{ij} + h^{tr}_{ij} + h^p_{ij}, \tag{28}$$

where h^e_{ij}, h^{tr}_{ij}, and h^p_{ij} stand for the components of the elastic, transformation, and plastic small strain tensors, respectively.

5.2.3 Elastic deformation and phase transformation

Assuming that phase transformation is a volume preserving process, the objective rate of the transformation strain tensor is taken as

$$\mathring{h}_{ij}^{tr} = \dot{\xi} H N_{ij}, \tag{29}$$

where the martensite volume fraction, ξ, is restricted by $0 \leq \xi \leq 1$, H is the measure of the effective transformation strain when $\xi = 1$, *i.e.*, $H = \sqrt{\frac{2}{3} h_{ij}^{tr} h_{ij}^{tr}}$, and the flow direction for transformation, N_{ij} ($\|N_{ij}\| = 1$), depends on the deviatoric Kirchhoff stress tensor, with components $\tau'_{ij} = \tau_{ij} - \frac{\tau_{kk}}{3}\delta_{ij}$ ($\tau_{ij} = J\sigma_{ij}$, where J is the Jacobian of the deformation, and σ_{ij} are the components of the Cauchy stress tensor).

The transformation direction

$$N_{ij} = \frac{3}{2}\frac{\tau'_{ij}}{\tau}, \tag{30}$$

is the normal to the transformation function

$$\Phi(\tau_{ij}, \xi) = \pi - Y \leq 0, \tag{31}$$

where

$$\pi = H\tau + \frac{1}{2}\tau_{ij}\Delta S_{ijkl}\tau_{kl} + \rho\Delta s_0 T - \Delta u_0 - \frac{1}{2}a_1\left[1 + \xi^{n_1} - (1-\xi)^{n_2}\right] - a_2, \tag{32}$$

is the thermodynamic force conjugate to martensite volume fraction, $Y > 0$ the critical value for the activation of transformation, s_0 and u_0 are the specific entropy and internal energy, respectively, ρ is the density, Δ denotes the difference in property

between the martensitic and the austenitic states, $\tau = \sqrt{\frac{3}{2}\tau'_{ij}\tau'_{ij}}$ stands for the effective Kirchhoff stress. $S_{ijkl} = (1-\xi)S^A_{ijkl} + \xi S^M_{ijkl}$, is the effective compliance tensor evaluated by the rule of mixtures, where S^A_{ijkl} and S^M_{ijkl} are the components of the compliance tensor of austenite and martensite, respectively, assumed isotropic, *i.e.*, $S^\alpha_{ijkl} = \frac{1+\nu_\alpha}{2E_\alpha}(\delta_{il}\delta_{jk} + \delta_{ik}\delta_{jl}) - \frac{\nu_\alpha}{E_\alpha}\delta_{ij}\delta_{kl}$, where E_α, ν_α denote the Young modulus and Poisson ratio, respectively, and the index α stands for A in the case of austenite and for M in the case of martensite. The various model parameters introduced above are given in terms of the common material properties that are used to calibrate the constitutive models of SMAs, H, M_s, M_f, and C_M, where C_M is the Clapeyron slope for forward transformation (Figure 28). The exponents n_1 and n_2 are chosen to best fit the observed transformation-induced hardening response. The calibration procedure is described in detail in [181]. The relations between the material and model parameters are given in Table 2.

Table 2: Connection between model parameters and the material parameters.

$\rho\Delta s_0 = -HC^M$
$\rho\Delta u_0 = \rho\Delta s_0 M_s$
$a^t_1 = \rho\Delta s_0(M_f - M_s)$
$a^t_2 = -Y$

5.2.4 Plastic deformation

During plastic deformation of martensite, the objective plastic strain rate is given by

$$\mathring{h}^p_{ij} = \dot{\bar{h}}^p \frac{3}{2}\frac{\tau'_{ij}}{\bar{\tau}}, \tag{33}$$

Table 3: Parameter values used for the numerical results presented.

parameter	value	parameter	value
E_A [MPa]	62000	H	0.03
E_M [MPa]	22000	M_f [^{o}C]	-33
$\nu_A = \nu_M$	0.33	M_s [^{o}C]	-27
$\tau_{y_0}^M$ [MPa]	800	C_M [MPa ^{o}C^{-1}]	6
λ	1500	n_1 & n_2	0.9
n	0.33		

where $\dot{\bar{h}}^p = \sqrt{\frac{2}{3}\dot{h}_{ij}^p \dot{h}_{ij}^p}$ is the effective plastic strain rate, and the stress state satisfies the consistency condition, which is defined by the von Mises yield surface

$$f(\tau_{ij}, \bar{h}^p) = \bar{\tau} - \tau_y^M = 0. \tag{34}$$

Assuming isotropic hardening, the yield stress τ_y^M evolves as

$$\tau_y^M(\bar{h}^p) = \tau_{y_0}^M + \lambda \left(\bar{h}^p\right)^n, \tag{35}$$

where n and λ are fitting parameters, and $\bar{h}^p = \int d\bar{h}^p$ is the accumulated equivalent plastic strain.

5.3 Unit cell model for simulations

The axisymmetric void unit cell model, initially employed to investigate ductile fracture in elastic–plastic materials [83], is adopted. The unit cell is cylindrical, with initial length $2L_{z0}$ and diameter $2L_{r0}$, containing a spheroidal void at its center, with initial radii r_{z0} and r_{r0}. 248 four-node, linear axisymmetric finite elements (CAX4) are used for the discretization of one quarter of the axisymmetric cross section (Figure 29).

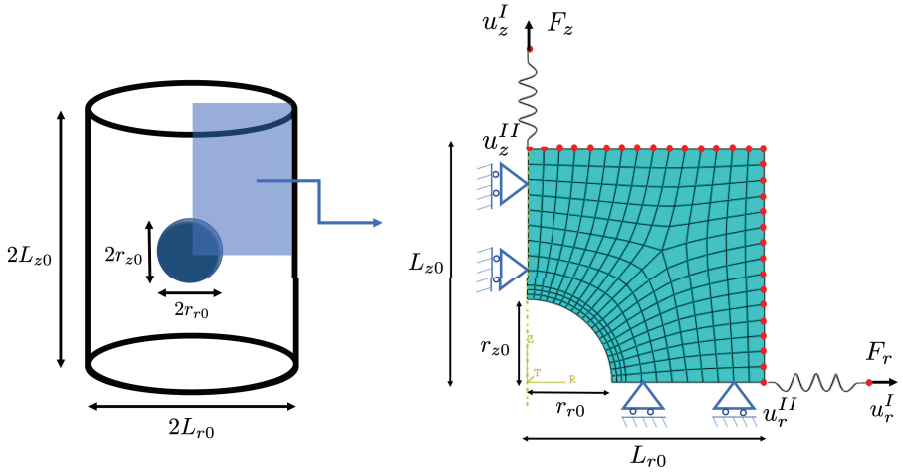

Figure 29: Axisymmetric unit cell and the boundary value problem solved in ABAQUS/STANDARD.

The boundary conditions constrain the cell external boundaries to remain straight and the stress triaxiality

$$T = \frac{\Sigma_m}{\Sigma_e} = \frac{1}{3}\left(\frac{1+2\rho}{1-\rho}\right), \tag{36}$$

to remain constant, where

$$\Sigma_m = \frac{1}{3}(\Sigma_{zz} + 2\Sigma_{rr}), \quad \Sigma_e = |\Sigma_{zz} - \Sigma_{rr}|, \tag{37}$$

stand for the volume-averaged mean and effective Cauchy stress, respectively, and $\rho = \Sigma_{zz}/\Sigma_{rr}$. The volume-averaged mesoscopic stress components Σ_{zz} and Σ_{rr} are calculated from the forces generated in the linearly elastic springs (Figure 29), $F_z = k\left(u_z^I - u_z^{II}\right)$ and $F_r = k\left(u_r^I - u_r^{II}\right)$ (k is the stiffness of the springs), respectively, which are constrained to deform such that $\Sigma_{zz} = \rho\Sigma_{rr}$ (see for details [152]).

The macroscopic effective logarithmic strains, E_{zz} and E_{rr}, read as

$$E_{zz} = \ln\left(\frac{L_z}{L_{z0}}\right), \quad E_{rr} = \ln\left(\frac{L_r}{L_{r0}}\right), \tag{38}$$

and the effective strain as

$$E_e = \frac{2}{3}|E_{zz} - E_{rr}|. \tag{39}$$

5.4 Results and discussion

The material parameters adopted in the numerical simulations are representative of near-equiatomic, precipitation-hardened NiTi SMAs [112]. The results presented below are at room temperature for three initial porosities, $f_0 = 2r_{z0}r_{r0}^2/(3L_{z0}L_{r0}^2)$, set as $f_0 = 0.001$, $f_0 = 0.03$ or $f_0 = 0.07$. The value 0.001 is assumed representative of the volume fraction of large second phase inclusions, such as oxides and carbides, and the values 0.03 and 0.07 representative of the volume fraction of precipitates [35]. In all simulations, the initial cell aspect ratio is set equal to one and the initial void aspect ratio, $w_0 = r_{z0}/r_{r0}$, is set as $w_0 = 1/4$, $w_0 = 1$ or $w_0 = 4$ to further investigate the effect of the lenticular geometry of precipitates on the cell response. The symbols $\circ$ and $\times$ in the figures correspond to the peak value of the volume-averaged effective stress Σ_e and the onset of void coalescence, which corresponds to plastic collapse in the intervoid ligament with elastic unloading away from the localization zone, respectively.

The numerical simulations reveal that void growth/coalescence due to combined phase transformation and plastic deformation proceeds in a manner similar to void growth/coalescence due to plastic deformation alone. At the onset of coalescence, the porosity increases rapidly, the void aspect ratio decreases rapidly, and the load drops abruptly. Coalescence of the voids occurs only by plastic localization due to the "finite" nature of the phase-transformation-induced strains. The point of coalescence is always at the descending part of the effective stress–effective strain curve, *i.e.*, past the peak stress points. More importantly for the present study, the strain at the

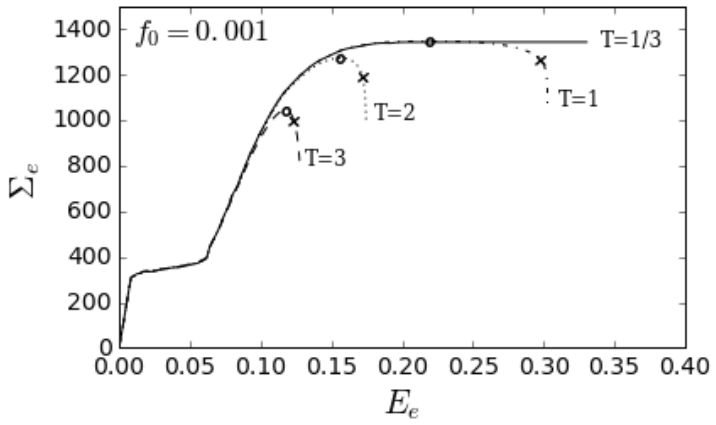

[a]

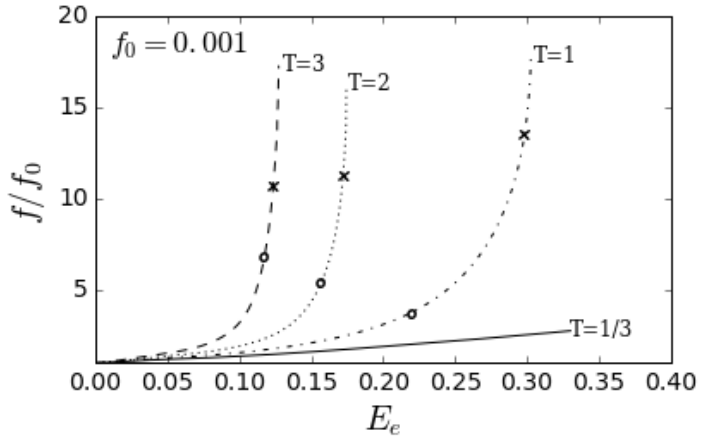

[b]

Figure 30: Figure 30[a] shows effective stress vs effective strain and Figure 30[b] shows porosity vs effective strain. This is cell response for $f_0 = 0.001$, $w_0 = 1$, and $T = 1/3, 1, 2, 3$.

peak volume-averaged effective stress increases with decreasing (i) stress triaxiality (Figures 30[a], 31[a], and 32[a]), (ii) initial porosity (Figures 30[a] vs 31[a] vs 32[a]), and (iii) cell aspect ratio or increasing (iv) plastic hardening and (v) initial aspect ratio for spheroidal voids (small aspect ratio refers to oblate and large aspect ratio to prolate spheroids) (Figure 33[a]). The ratio of the value of porosity corresponding to the peak stress over the initial porosity, f_p/f_0, follows the same trends with the exception of triaxiality and aspect ratio of the voids that do not show a monotonic trend (Figures 30[b], 31[b], 32[b], and Figure 33[b], respectively). These results are in accord with unit cell studies of elastic–plastic materials (see, *e.g.*, [21]); the ones

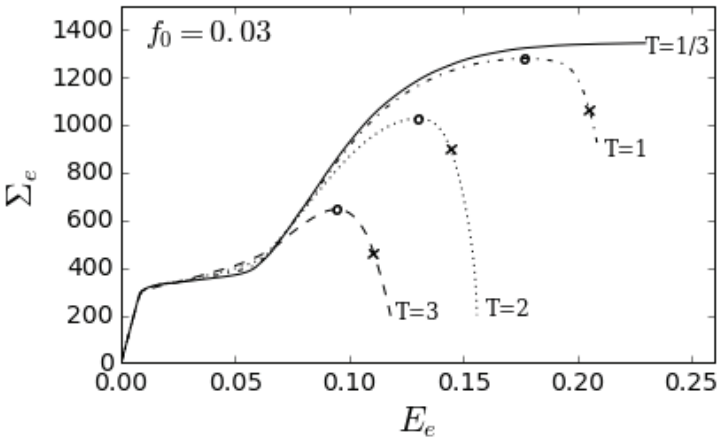

[a]

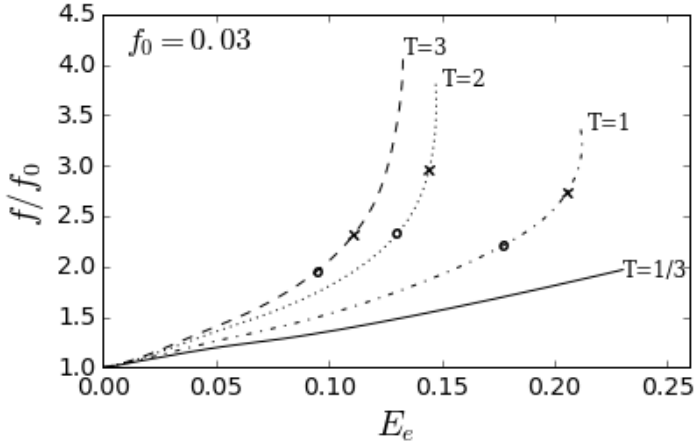

[b]

Figure 31: Figure 31[a] shows effective stress vs effective strain and Figure 31[b] shows porosity vs effective strain. This is cell response for $f_0 = 0.03$, $w_0 = 1$, and $T = 1/3, 1, 2, 3$.

related to the cell aspect ratio and plastic hardening are not presented herein for brevity. The ratio f_p/f_0 is the single most important value on the interpretation of the cell response on the fracture response of SMAs in the discussion below.

As already mentioned, phase transformation and large volume fractions of second phase particles differentiate SMAs from "conventional" intermetallics. Phase transformation has an impact on the f_p/f_0-value; the higher the transformation strain, the higher the f_p/f_0-value (Figures 34[b] and 35[b]). This impact is dependent on the initial void-volume fraction. The higher the initial void-volume fraction, the lower the effect of phase transformation (Figure 34[b] vs 35[b]). A detailed analysis of the

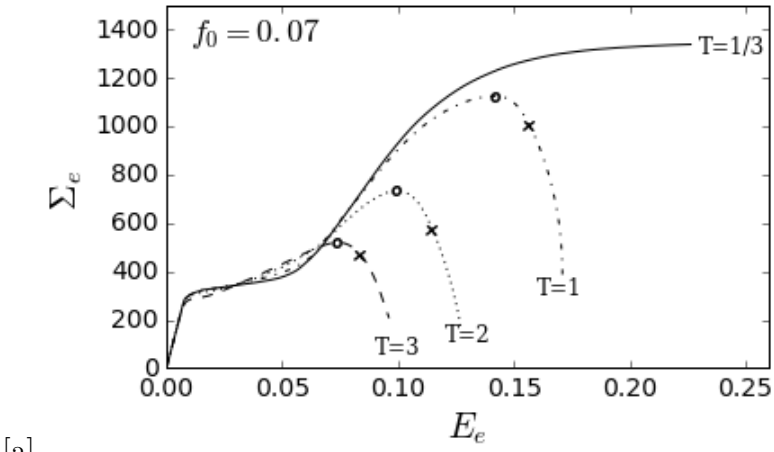

[a]

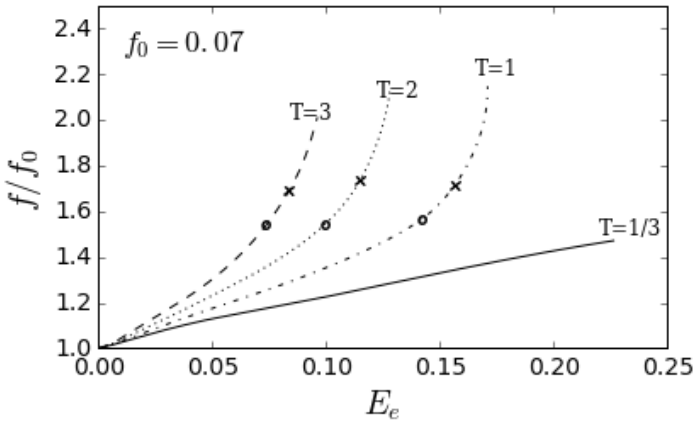

[b]

Figure 32: Figure 32[a] shows effective stress vs effective strain and Figure 32[b] shows porosity vs effective strain. This is cell response for $f_0 = 0.07$, $w_0 = 1$, and $T = 1/3, 1, 2, 3$.

combined effect of phase transformation and plastic deformation on the evolution of porosity is omitted here as it is similar to that presented in [67] (Section 3.3), which describes void growth and coalescence in porous elastic–plastic solids with sigmoidal hardening, *i.e.*, materials with a double stage hardening and saturation response; a phenomenological response which is very similar to that of SMAs.

Combining the unit cell studies with the experimental observations in [122], the following hypotheses can be made regarding void growth and coalescence in SMAs.

Void Coalescence.– The available experimental data on notched round-bars indicate that precipitation-hardened SMAs do not exhibit a softening response prior to

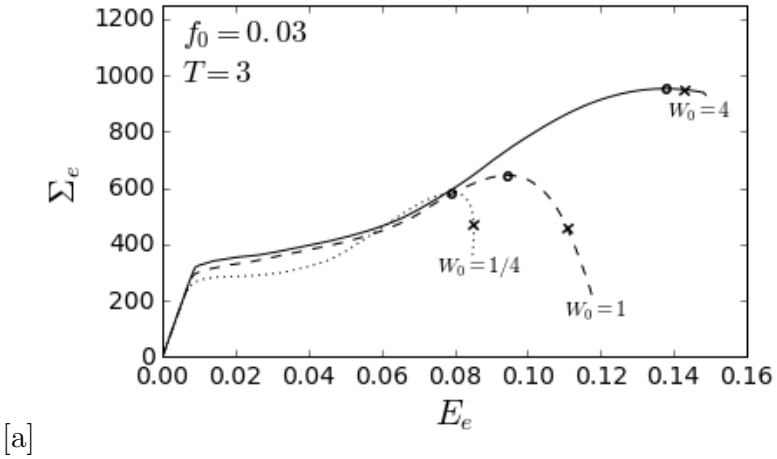

[a]

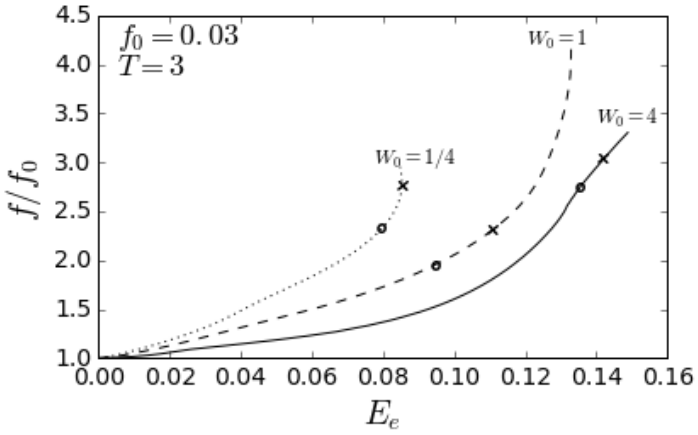

[b]

Figure 33: Figure 33[a] shows effective stress vs effective strain and Figure 33[b] shows porosity vs effective strain. This is cell response for $f_0 = 0.03$, $w_0 = 1/4, 1, 4$, and $T = 3$.

failure. Given that void coalescence always occurs past the maximum-stress points on the effective stress–effective strain curve, it is reasonable to assume that flow localization in the intervoid ligaments is limited and that void initiation/growth is mostly followed by cleavage.

Void Growth.– Void nucleation aside, assuming that the initial porosity corresponds to the volume fraction of inclusions, the maximum extent of void growth expected can be characterized by the ratio between the porosity value at peak stress and the initial value, *i.e.*, f_p/f_0. The porosity that corresponds to the peak stress, f_p, is dependent on stress triaxiality, cell and void aspect ratio, plastic hardening, transformation

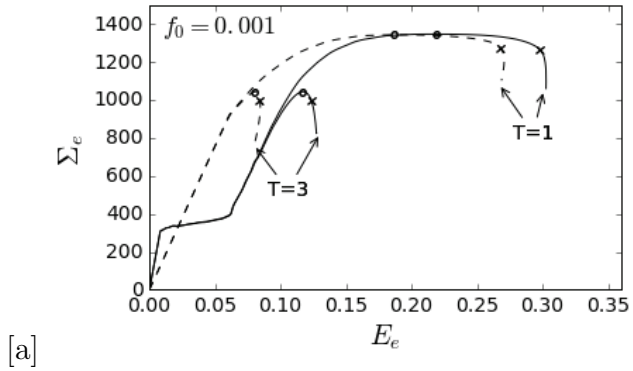

[a]

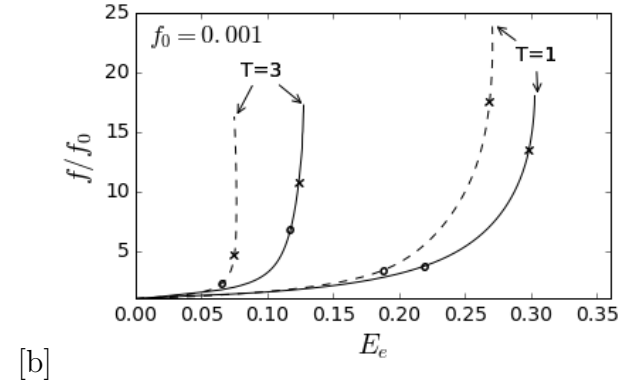

[b]

Figure 34: Figure 34[a] shows effective stress vs effective strain and Figure 34[b] shows porosity vs effective strain. Cell response for $f_0 = 0.001$, $w_0 = 1$, and $T = 1, 3$. The solid line corresponds to the SMA and the dashed line to the zero transformation SMA.

characteristics, and initial porosity. The most pronounced dependence is that on the initial porosity, f_0. The higher the initial porosity, f_0, the less important the void growth. For $f_0 = 0.03$, which is a relatively conservative estimate of the volume fraction of precipitates (around $2 \sim 7\%$ depending on aging [35]), the numerical results, which are representative of an SMA material (maximum transformation strain $3 \sim 6\%$), show a porosity growth at the peak effective stress value of less than 2.8, *i.e.*, $f_p/f_0 < 2.8$ (Figures 31[b], 33[b], and 35[b]). Thus, it can be safely assumed that no pronounced void growth is expected in precipitation-hardened SMAs due the high volume fraction of precipitates as compared to conventional ductile materials, in which porosity growth is at least an order of magnitude greater due to the combined effects of (i) their low initial porosities (compared to precipitation-hardened SMAs),

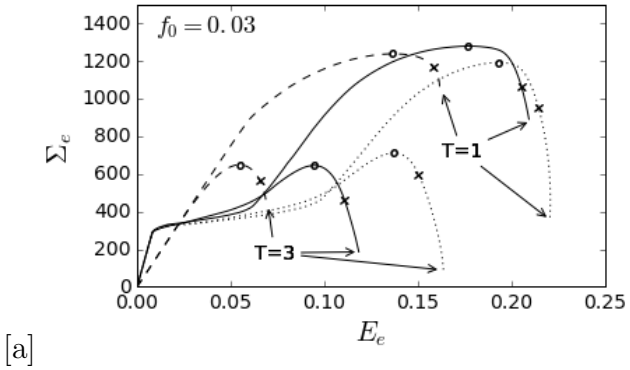

[a]

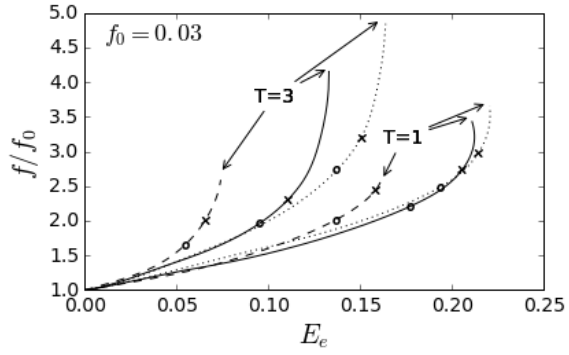

[b]

Figure 35: Figure 35[a] shows effective stress vs effective strain and Figure 35[b] shows porosity vs effective strain. The solid line corresponds to the SMA, the dashed line to the zero transformation, and dotted line for SMA material with double its maximum transformation strain, *i.e.*, $H = 0.06$.

and (ii) coalescence.

In conclusion, it is conjectured that void nucleation and cleavage should dominate the fracture response of SMAs due to the high volume fraction of precipitates in SMAs and the limited flow localization observed in experiments [159]. It is expected that the voids first initiate at large second phase particles, such as $NiTi_2$, carbides, and oxides [79]. The stress field of the large voids favors the nucleation of voids from the precipitates [59, 158], which nucleate and grow preferentially near such particles and grain boundaries [43]. However, given the high volume fraction of precipitates as compared to that of larger inclusions (and not the other way around), the distribution of void sizes should not alter significantly the simulated void growth kinetics prior to the peak effective-stress value. Unit cell studies, in the realm of [120, 44, 84, 151], are

expected to shed light in the void nucleation process, in which phase transformation, contrary to void growth and coalescence, should play a more significant role.

6 Discussion & conclusions.

Since their discovery, the research focus of shape memory alloys (SMAs) has been to take advantage of their key properties, such as pseudoelasticity and shape memory effect, into engineering applications, starting from the biomedical to the aerospace, outer-space, and automotive industries among others. In order for SMAs to fulfill their potential in commercial actuation, vibration damping and energy absorption applications, proper fracture mechanics concepts should be established and promoted to ensure structural integrity and performance assurance. SMAs display slow and stable crack growth due to the dissipative and hysteric nature of their deformation response, similarly to conventional ductile metals, although the fracture micromechanisms are characterized by cleavage in conjunction with ductile tearing.

The research presented in this dissertation on the fracture response of SMAs has culminated to the following.

- Required modifications to ASTM standards for the experimental measurement of fracture toughness (isothermal loading conditions)

  - SMAs display slow and stable crack advance and require a crack extension resistance curve, R-curve, to be measured for characterizing their fracture response. Due to the non-linearity of their deformation response, a J-integral vs crack growth plot description of the R-curve behavior is preferable in terms of fracture specimen size; a K-based description may require prohibitively large specimen. Basic assumptions of the ASTM methodology, developed for conventional ductile materials, for constructing the R-curve and determining a thickness-independent fracture toughness do not comply with the fracture and deformation response of SMAs. Proposed modifications to ASTM standards and other concluding results are

summarized below:

- Measurement of J^{el} by multiplying the elastic area under the load–load line displacement by a configuration-dependent η^{el}-factor for static cracks and a correction for advancing cracks. Such measurements are expected to result in J_{I_C}-values that are higher than the ones determined by following the ASTM standards, but not in excess of 10% difference. The difference in the tearing modulus, *i.e.*, the J–Δa slope, with implications on the tearing stability, which is of interest in structural applications, is expected to be of the same order.
- Construction/exclusion/offset lines of a slope much higher than the default value recommended in ASTM standards would be more realistic in determining the J_{I_C}-value on the J_R-curve given that crack-tip blunting in SMAs is not as pronounced as in conventional ductile materials.
- SMAs fail predominantly by cleavage and thus the ASTM thickness requirement for conventional ductile materials is far more stringent than is necessary to ensure a constraint-independent fracture toughness measurement.
- The fracture toughness measurements at temperatures below M_d should be considered representative of martensite and those above M_d of austenite. Temperature may be an extra source of variability in measured J_{I_C}-values below M_d due to their dependence on the elastic properties of the stable phase, which may be either martensite at temperatures at which martensite is stable or austenite in the pseudoelastic temperature range. Extrapolated $K_{J_{I_C}}$-values are independent of the elastic properties and thus independent of temperature within the range of interest for SMAs.
- The elastic compliance method can accurately estimate the crack length

due to the mild dependence of the related calculations on the Young's modulus. But does this method provides accuracy is a question that can be answered through experimental observations because phase transformation is a reversible process and unloading can apparently lead to reversal of transformation toughening as it causes divergence from the master curve as we start to reload again thus reports lower fracture toughness values.

  - Presented isothermal fracture toughness experiments suggest that the driving force required for crack advance in superelastic SMAs can be altered through simple unloading, *i.e.*, the transformation toughening associated with crack advance is reversible. This response is attributed to the impact of reverse phase transformation on the crack tip strain field in an unloading/reloading cycle and has implications on the evaluation and range of validity of the resistance curve. An R-curve measured according to the ASTM standards may no longer be treated as a "material property" since it may substantially differ from an R-curve response under monotonic loading. Thus, the ability of an R-curve obtained according to the standards to describe effectively resistance against stable growth and tearing instability is rather constrained, which limits its applicability in practical engineering, *e.g.*, fitness-for-service evaluation or structural integrity assessment for engineering components and structures.

- Experimental fracture toughness measurements under actuation loading conditions

  - Isobaric actuation fracture toughness experiments were able to present a one-parameter interpretation of the experimental data obtained from SMAs under coupled thermo-mechanical loading. The interpretation of the data is based on an approximation of the value of a path-independent

contour integral by the load–load line displacement record measured. The obtained results, which represent the first experimental measurement of the fracture toughness of SMAs under actuation loading conditions, suggest that (i) the employed contour integral should achieve similitude for a wide range of thermomechanical loading conditions and geometric configurations, and that (ii) isothermal conditions provide a more pronounced toughness enhancement as compared to thermal loading under a constant bias load.

- On the relative importance of cleavage and ductile tearing

  - Unit cell studies were conducted to study void growth in SMAs in an effort to address the importance of ductile rupture in the overall failure response of these materials. The unit cell consists of a single pre-existing void, assumed to have initiated from a second phase particle, embedded in a SMA matrix material. The numerical simulations, which were representative of a near-equiatomic precipitation-hardened NiTi, and experimental evidence, which suggests that the macroscopic crack initiation is stress-driven, indicate that the fracture response is dominated by void initiation and cleavage with void growth playing a secondary/minor role due to the precipitates' high volume fraction.

References

[1] A. Ahadi and Q. Sun. Grain Size Dependence of Fracture Toughness and Crack-Growth Resistance of Superelastic NiTi. *Scripta Materialia*, 113:171–175, 2016.

[2] S.N. Alturi. Energetic approaches and path-independent integrals in fracture mechanics. In S.N. Alturi, editor, *Computational methods in the mechanics of fracture*, chapter 5, pages 121–165. North-Holland, Amsterdam, 1986.

[3] G.F. Andreasen and T.B. Hilleman. An evaluation of 55 cobalt substituted nitinol wire for use in orthodontics. *The Journal of the American Dental Association*, 82(6):1373–1375, 1971.

[4] ASTM-E1820. Standard Test Method for Measurement of Fracture Toughness. Technical report, ASTM International, West Conshohocken, PA, 2016.

[5] H. Bahrami, S.H. Hoseini, and G.Z. Voyiadjis. Fracture analysis of shape memory alloys in martensite and austenite phase based on the voids behavior. *Mech. Mater.*, 137:103119, 2019.

[6] H. Bahrami, S.H. Hoseini, and G.Z. Voyiadjis. Fracture investigation of the shape memory alloy using GTN model. *Engng Fract. Mech.*, 216:106519, 2019.

[7] S. Barbarino, S. Flores, R.M. Ajaj, I. Dayyani, and M.I. Friswell. A review on shape memory alloys with applications to morphing aircraft. *Smart Mater. Struct.*, 23(6):063001, 2014.

[8] B. Barnes, D. Brei, J. Luntz, A. Browne, and K. Strom. Panel deployment using ultrafast sma latches. In *ASME International Mechanical Engineering Congress and Exposition*, volume 47659, pages 273–280, 2006.

[9] T. Baxevanis, Y. Chemisky, and D.C. Lagoudas. Finite Element Analysis of The Plane Strain Crack-tip Mechanical Fields in Pseudoelastic Shape Memory Alloys. *Smart Materials and Structures*, 21(9):094012, 2012.

[10] T. Baxevanis, Y. Chemisky, and D.C. Lagoudas. Finite element analysis of the plane-strain crack-tip mechanical fields in pseudoelastic shape memory alloys. *Smart Mater. Struct.*, 21(9):094012, 2012.

[11] T. Baxevanis and D. Lagoudas. A Mode I Fracture Analysis of a Center-Cracked Infinite Shape Memory Alloy Plate Under Plane Stress. *International Journal of Fracture*, pages 1–16, 2012.

[12] T. Baxevanis and D. Lagoudas. A mode I fracture analysis of a center-cracked infinite shape memory alloy plate under plane stress. *Int. J. Fract.*, 175(2):151–166, 2012.

[13] T. Baxevanis and D. C. Lagoudas. Fracture mechanics of shape memory alloys: review and perspectives. *Int. J. Fract.*, 191:191–213, 2015.

[14] T. Baxevanis and D.C. Lagoudas. Fracture Mechanics of Shape Memory Alloys: Review and Perspectives. *International Journal of Fracture*, 191(1-2):191–213, 2015.

[15] T. Baxevanis, C.M. Landis, and D.C. Lagoudas. On the effect of latent heat on the fracture toughness of pseudoelastic shape memory alloys. *J. Appl. Mech., Transactions ASME*, 81(10), 2014. doi: 10.1115/1.4028191.

[16] T. Baxevanis, C.M. Landis, and D.C Lagoudas. On the Fracture Toughness of Pseudoelastic Shape Memory Alloys. *Journal of Applied Mechanics*, 81(4):041005, 2014.

[17] T. Baxevanis, C.M. Landis, and D.C. Lagoudas. On the Fracture Toughness of Pseudoelastic Shape Memory Alloys. *Journal of Applied Mechanics*, 81(4):041005, 2014.

[18] T. Baxevanis, A. Parrinello, and C.D. Lagoudas. On the driving force for crack growth during thermal actuation of shape memory alloys. *J. Mech. Phys. Solids*, 89:255–271, 2016.

[19] T. Baxevanis, A. Parrinello, and D.C. Lagoudas. On the fracture toughness enhancement due to stress-induced phase transformation in shape memory alloys. *Int. J. Plast.*, 50:158–169, 2013.

[20] T. Baxevanis, A.F. Parrinello, and D.C. Lagoudas. On the Driving Force for Crack Growth During Thermal Actuation of Shape Memory Alloys. *Journal of the Mechanics and Physics of Solids*, 89:255–271, 2016.

[21] A.A. Benzerga and Jean-Baptiste Leblond. Ductile fracture by void growth to coalescence. In Hassan Aref and Erik van der Giessen, editors, *Advances in Applied Mechanics*, volume 44 of *Advances in Applied Mechanics*, pages 169–305. 2010.

[22] V. Birman. On mode i fracture of shape memory alloy plates. *Smart materials and structures*, 7(4):433, 1998.

[23] V. Brailovski and F. Trochu. Review of shape memory alloys medical applications in russia. *Bio-medical materials and engineering*, 6(4):291–298, 1996.

[24] B. Budiansky, J.W. Hutchinson, and J.C. Lambropoulos. Continuum theory of dilatant transformation toughening in ceramics. *International Journal of Solids and Structures*, 19(4):337–355, 1983.

[25] B. Budiansky, J.W. Hutchinson, and S. Slutsky. Void growth and collapse in viscous solids. In H.G. Hopkins and M.J. Sewell, editors, *Mech. Solids*, pages 13–45. Pergamon, Oxford, 1982.

[26] W.J. Buehler, J. V. Gilfrich, and R.C. Wiley. Effect of low-temperature phase changes on the mechanical properties of alloys near composition tini. *Journal of applied physics*, 34(5):1475–1477, 1963.

[27] J.H. Chen, G.Z. Wang, and W. Sun. Investigation on the fracture behavior of shape memory alloy niti. *Metallurgical and Materials Transactions A*, 36(4):941–955, 2005.

[28] C. Chu and A. Needleman. Void nucleation effects in biaxially stretched sheets. *J. Engng Mat. Techn.*, 102:249–256, 1980.

[29] G.A. Clarke, W.R. Andrews, P.C. Paris, and D.W. Schmidt. Single Specimen Tests for J_{Ic} Determination. In *Mechanics of Crack Growth*. ASTM International, 1976.

[30] G.A. Clarke and J.D. Landes. Evaluation of the J Integral for The Compact Specimen. *Journal of Testing and Evaluation*, 7(5):264–269, 1979.

[31] A. Creuziger, L.J. Bartol, K. Gall, and W.C. Crone. Fracture in single crystal NiTi. *J. Mech. Phys. Solids*, 56:2896–2905, 2008.

[32] S. Daly, A. Miller, G. Ravichandar, and K. Bhattacharya. An experimental investigation of crack initiation in thin sheets of nitinol. *Acta Mater.*, 55:6322–6330, 2007.

[33] M.R. Daymond, M.L. Young, J.D. Almer, and D.C. Dunand. Strain and texture evolution during mechanical loading of a crack tip in martensitic shape-memory niti. *Acta Materialia*, 55(11):3929–3942, 2007.

[34] R.H. Dean and J.W. Hutchinson. Quasi-static steady crack growth in small scale yielding. In *Fracture Mechanics*, ASTM-STP 700, pages 383–405, 1980.

[35] A. Dlouhý, J. Khalil-Allafi, and G. Eggeler. On the determination of the volume fraction of Ni_4Ti_3 precipitates in binary Ni-rich NiTi shape memory alloys. *Zeitschrift f ur Metallkunde*, 95(6):518–524, 2004.

[36] W.J. Drugan, J.R. Rice, and T-L. Sham. Asymptotic analysis of growing plane strain tensile cracks in elastic-ideally plastic solids. *Journal of the Mechanics and Physics of Solids*, 30(6):447–473, 1982.

[37] T.W. Duerig. Superelastic nitinol for medical device. *Medical Plastics and Biomaterials.*, pages 31–42, 1997.

[38] T.W. Duerig, K.N. Melton, and D.W.C.M. Stöckel. *Engineering aspects of shape memory alloys*. Butterworth-heinemann, 2013.

[39] G. Eggeler, E. Hornbogen, A. Yawny, A. Heckmann, and M. Wagner. Structural and functional fatigue of NiTi shape memory alloys. *Materials Science and Engineering: A*, 378(1):24–33, 2004.

[40] H. Ernst, P.C. Paris, M. Rossow, and J.W. Hutchinson. Analysis of Load-Displacement Relationship to Determine JR Curve and Tearing Instability Material Properties. In *Fracture Mechanics: Proceedings of the Eleventh National Symposium on Fracture Mechanics: Part I*. ASTM International, 1979.

[41] H.A. Ernst, P.C. Paris, and J.D. Landes. Estimations on J-integral and Tearing Modulus T from a Single Specimen Test Record. In *Fracture Mechanics*. ASTM International, 1981.

[42] A.G. Evans and R.M. Cannon. Overview no. 48. Toughening of brittle solids by martensitic transformations. *Acta Metallurgica*, 34(5):761–800, 1986.

[43] P. Filip and K. Mazanec. On precipitation kinetics in TiNi shape memory alloys. *Scripta Mater.*, 45(6):701–707, 2001.

[44] N.A. Fleck, J.W. Hutchinson, and V. Tvergaard. Softening by void nucleation and growth in tension and shear. *J. Mech. Phys. Solids*, 37(4):515–540, 1989.

[45] Y. Freed and L. Banks-Sills. Crack Growth Resistance of Shape Memory Alloys by Means of a Cohesive Zone Model. *Journal of the Mechanics and Physics of Solids*, 55(10):2157–2180, 2007.

[46] Y. Freed and L. Banks-Sills. Crack growth resistance of shape memory alloys by means of a cohesive zone model. *J. Mech. Phys. Solids*, 55:2157–2180, 2007.

[47] H. Funakubo and J.B. Kennedy. Shape memory alloys. *Gordon and Breach, xii+ 275, 15 x 22 cm, Illustrated*, 1987.

[48] K. Gall, H. Sehitoglu, Y.I. Chumlyakov, Y.L. Zuev, and I. Karaman. The role of coherent precipitates in martensitic transformations in single crystal and polycrystalline ti-50.8 at% ni. *Scripta materialia*, 39(6):699–705, 1998.

[49] K. Gall, N. Yang, H. Sehitoglu, and Y. I. Chumlyakov. Fracture of precipitated NiTi shape memory alloys. *Int. J. Fract.*, 109:189–207, 1998.

[50] K. Gall, N. Yang, H. Sehitoglu, and Y.I. Chumlyakov. Fracture of precipitated niti shape memory alloys. *International journal of fracture*, 109(2):189–207, 2001.

[51] K. Gall, N. Yang, H. Sehitoglu, and Y.I. Chumlyakov. Fracture of precipitated NiTi shape memory alloys. *International Journal of Fracture*, 109:189–207, 2001.

[52] O.J. Godard, M.Z. Lagoudas, and D.C. Lagoudas. Design of space systems using shape memory alloys. In *Smart Structures and Materials 2003: Smart Structures and Integrated Systems*, volume 5056, pages 545–558. International Society for Optics and Photonics, 2003.

[53] S. Gollerthan, M. L. Young, A. Baruj, J. Frenzel, W.W. Schmahl, and G. Eggeler. Fracture mechanics and microstructure in NiTi shape memory alloys. *Acta Materialia*, 57:1015–1025, 2009.

[54] S. Gollerthan, M.L. Young, A. Baruj, J. Frenzel, W.W. Schmahl, and G. Eggeler. Fracture Mechanics and Microstructure in NiTi Shape Memory Alloys. *Acta Materialia*, 57(4):1015–1025, 2009.

[55] S. Gollerthan, M.L. Young, K. Neuking, U. Ramamurty, and G. Eggeler. Direct Physical Evidence for the Back-Transformation of Stress-Induced Martensite in the Vicinity of Cracks in Pseudoelastic NiTi Shape Memory Alloys. *Acta Materialia*, 57(19):5892–5897, 2009.

[56] A. L. Gurson. Continuum Theory of Ductile Rupture by Void Nucleation and Growth: Part I. Yield Criteria and Flow Rules for Porous Ductile Media. *J. Engng Mater. Tech.*, 99(1):2–15, 1977.

[57] B. Haghgouyan, C. Hayrettin, T. Baxevanis, I. Karaman, and D.C. Lagoudas. Fracture toughness of niti–towards establishing standard test methods for phase transforming materials. *Acta Materialia*, 162:226–238, 2019.

[58] B. Haghgouyan, C. Hayrettin, T. Baxevanis, I. Karaman, and D.C. Lagoudas. Fracture toughness of NiTi: Towards establishing standard test methods for phase transforming materials. *Acta Materialia*, 162:226–238, 2019.

[59] J.W. Hancock and A.C. Mackenzie. On the mechanisms of ductile failure in high-strength steels subjected to multi-axial stress-states. *Journal of the Mechanics and Physics of Solids*, 24(2-3):147–160, 1976.

[60] C. Hayrettin, S. Jape, B. Young, T. Baxevanis, C.D. Lagoudas, and I. Karaman. Actuation-Induced Stable Crack Growth in Near-Equiatomic NiTi Shape Memory Alloys: Experimental and Numerical Analysis. 2019. submitted.

[61] S. Hazar, W. Zaki, Z. Moumni, and G. Anlas. Modeling of steady-state crack growth in shape memory alloys using a stationary method. *Int. J. Plastic.*, 67:26–38, 2015.

[62] H. Hencky. Uber die form des elastizitatsgesetzes bei ideal elastischen stoffen. *Zeit. Tech. Phys.*, 9:215–220, 1928.

[63] J. Hutchinson and P. Paris. Stability Analysis of J-Controlled Crack Growth. In *Elastic-Plastic Fracture*. ASTM International, 1979.

[64] J.W. Hutchinson. On steady quasi-static crack growth. Technical Report DEAP S-8, Division of Applied Sciences, Harvard University, 1974.

[65] A.P. Iliopoulos, J.C. Steuben, T. Kirk, T. Baxevanis, J.G. Michopoulos, and D.C. Lagoudas. Thermomechanical Failure Response of Notched NiTi Coupons. *International Journal of Solids and Structures*, 125:265–275, 2017.

[66] A. Illiopoulos, J. Steuben, T. Kirk, T. Baxevanis, J. Michopoulos, and C.D. Lagoudas. Thermomechanical failure response of notched NiTi coupons. *International Journal of Solids and Structures*, 125:265–275, 2017.

[67] P.P. Indurkar and S.P. Joshi. Void Growth and Coalescence in Porous Plastic Solids With Sigmoidal Hardening. *J. Appl. Mech.*, 86(9), 2019.

[68] CM Jacson. 55-nitinol-the alloy with a memory: its physical metallurgy, properties and applications. *NASA-SP-5110*, 15, 1972.

[69] J.M. Jani, M. Leary, A. Subic, and M.A. Gibson. A review of shape memory alloy research, applications and opportunities. *Materials & Design*, 56:1078–1113, 2014.

[70] S. Jape, T. Baxevanis, and C.D. Lagoudas. Stable crack growth during thermal actuation of shape memory alloys. *Shape Memory and Superelasticity*, 2:104–113, 2016.

[71] S. Jape, T. Baxevanis, and D.C. Lagoudas. Stable Crack Growth During Thermal Actuation of Shape Memory Alloys. *Shape Memory and Superelasticity*, 2(1):104–113, 2016.

[72] S. Jape, T. Baxevanis, and D.C. Lagoudas. Stable crack growth during thermal actuation of shape memory alloys. *Shape Mem. Super.*, 2(1):104–113, 2016.

[73] S. Jape, T. Baxevanis, and D.C. Lagoudas. On the fracture toughness and stable crack growth in shape memory alloy actuators in the presence of transformation-induced plasticity. *Int. J. Fract.*, 209:117–130, 2017.

[74] S. Jape, T. Baxevanis, and D.C. Lagoudas. On the fracture toughness and stable crack growth in shape memory alloy actuators in the presence of transformation-induced plasticity. *International Journal of Fracture*, 209(1):117–130, 2018.

[75] S. Jape, B. Young, B. Haghgouyan, C. Hayrettin, T. Baxevanis, D.C. Lagoudas, and I. Karaman. Actuation-induced stable crack growth in near-equiatomic nickel-titanium shape memory alloys: Experimental and numerical analysis. *International Journal of Solids and Structures*, 2020.

[76] S. Jape, B. Young, B. Haghgouyan, C. Hayrettin, T. Baxevanis, D.C. Lagoudas, and I. Karaman. Actuation-induced stable crack growth in near-equiatomic nickel-titanium shape memory alloys: Experimental and numerical analysis. *International Journal of Solids and Structures*, 221:165–179, 2021.

[77] D. Jiang and C.M. Landis. A constitutive model for isothermal pseudoelasticity coupled with plasticity. *Shape Mem. Super.*, 2(4):360–370, 2016.

[78] J.A. Joyce and J.P. Gudas. Computer Interactive J_{Ic} of Testing Navy Alloys. In *Elastic-Plastic Fracture*. ASTM International, 1979.

[79] M. Karlík, P. Haušild, J. Adámek, J. Drahokoupil, P. Novák, and L. Perrière. Microstructure of Ni-48 at.% Ti Alloy Prepared from Powder and by Conventional Metallurgy. *Acta Phys. Polonica, A.*, 134(3), 2018.

[80] J. Robert Kelly and Isabelle Denry. Stabilized zirconia as a structural ceramic: An overview. *Dental Materials*, 24(3):289–298, 2008.

[81] S.M. Keralavarma, S. Hoelscher, and A.A. Benzerga. Void growth and coalescence in anisotropic plastic solids. *Int. J. Solids Struct.*, 48(11):1696–1710, 2011.

[82] J. Khalil-Allafi, G. Eggeler, A. Dlouhy, W.W. Schmahl, and C. Somsen. On the influence of heterogeneous precipitation on martensitic transformations in a ni-rich niti shape memory alloy. *Materials Science and Engineering: A*, 378(1-2):148–151, 2004.

[83] J. Koplik and A. Needleman. Void growth and coalescence in porous plastic solids. *Int. J. Solids Struct.*, 24(8):835–853, 1988.

[84] M. Kuna and D. Z. Sun. Three-dimensional cell model analyses of void growth in ductile materials. *Inter. J. Fract.*, 81(3):235–258, 1996.

[85] G.V. Kurdjumov and L.G. Khandros. First reports of the thermoelastic behaviour of the martensitic phase of au-cd alloys. *Doklady Akademii Nauk SSSR*, 66(1949):211–213, 1949.

[86] G. Lacroix, T. Pardoen, and P.J. Jacques. The fracture toughness of TRIP-assisted multiphase steels. *Acta Materialia*, 56(15):3900–3913, 2008.

[87] D. Lagoudas, D. Hartl, Y. Chemisky, L. Machado, and P. Popov. Constitutive model for the numerical analysis of phase transformation in polycrystalline shape memory alloys. *International Journal of Plasticity*, 32–33:155–183, 2012.

[88] D.C. Lagoudas. *Shape Memory Alloys: Modeling and Engineering Applications*. Springer US, 2008.

[89] D.C. Lagoudas, editor. *Shape Memory Alloys: Modelling and Enginnering Applications*. Springer, New-York, 2008.

[90] D.C. Lagoudas and E.L. Vandygriff. Processing and characterization of niti porous sma by elevated pressure sintering. *Journal of intelligent material systems and structures*, 13(12):837–850, 2002.

[91] C.M. Landis. On the fracture toughness of ferroelastic materials. *Journal of the Mechanics and Physics of Solids*, 51(8):1347–1369, 2003.

[92] F.F. Lange. Transformation toughening - Part 2 Contribution to fracture toughness. *Journal of Materials Science*, 17(1):235–239, 1982.

[93] J. Lemaitre. Local approach of fracture. *Engng Fract. Mech.*, 25(5):523–537, 1986.

[94] C. Lexcellent and F. Thiebaud. Determination of the phase transformation zone

at a crack tip in a shape memory alloy exhibiting asymmetry between tension and compression. *Scripta Materialia*, 59(3):321–323, 2008.

[95] F.Z. Li, C.F. Shih, and A. Needleman. A comparison of methods for calculating energy release rates. *Enineering Fracture Mechanics*, 21:405–421, 1985.

[96] C. Liang, F.M. Davidson, L.M. Schetky, and F.K. Straub. Applications of torsional shape memory alloy actuators for active rotor blade control: opportunities and limitations. In *Smart Structures and Materials 1996: Smart Structures and Integrated Systems*, volume 2717, pages 91–100. International Society for Optics and Photonics, 1996.

[97] D.S. Lieberman, M.A. Schmerling, R.S. Karz, and J. Perkins. Shape memory effects in alloys. *Plenum, Press, New York*, page 203, 1975.

[98] A.F. Liu. *Mechanics and mechanisms of fracture: an introduction*. ASM International, 2005.

[99] G.M. Loughran, T.W. Shield, and P.H. Leo. Fracture of shape memory CuAlNi single crystals. *Int. J. Solids Struct.*, 40(2):271–294, 2003.

[100] L.G. Machado and M.A. Savi. Medical applications of shape memory alloys. *Brazilian journal of medical and biological research*, 36(6):683–691, 2003.

[101] J. Makkar and T. Baxevanis. Notes on the experimental measurement of fracture toughness of shape memory alloys. *Journal of Intelligent Material Systems and Structures*, 31(3):475–483, 2020.

[102] J. Makkar and T. Baxevanis. Notes on the experimental measurement of fracture toughness of shape memory alloys. *Journal of Intelligent Material Systems and Structures*, 31(3):475–483, 2020.

[103] J. Makkar and T. Baxevanis. On the fracture response of shape memory alloys by void growth and coalescence. *Mechanics of Materials*, 153:103682, 2021.

[104] J. Makkar, B. Young, I. Karaman, and T. Baxevanis. Experimental observations of "reversible" transformation toughening. *Scripta Materialia*, 191:81–85, 2021.

[105] C. Maletta. A novel fracture mechanics approach for shape memory alloys with trilinear stress-strain behavior. *Int. J. Fract.*, 177(1):39–51, 2012.

[106] C. Maletta and F. Furgiuele. Analytical modeling of stress-induced martensitic transformation in the crack tip region of nickel–titanium alloys. *Acta Materialia*, 58(1):92–101, 2010.

[107] C. Maletta and F. Furgiuele. Analytical modeling of stress-induced martensitic transformation in the crack tip region of nickel-titanium alloys. *Acta Mater.*, 58:92–101, 2010.

[108] C. Maletta, E. Sgambitterra, and F. Niccoli. Temperature dependent fracture properties of shape memory alloys: Novel findings and a comprehensive model. *Scientific Reports*, 6, 2016.

[109] C. Maletta and M.L. Young. Stress-induced martensite in front of crack tips in niti shape memory alloys: modeling versus experiments. *Journal of materials engineering and performance*, 20(4):597–604, 2011.

[110] D. B. Marshall. Strength characteristics of transformation-toughened zirconia. *Journal of the American Ceramic Society*, 69(3):173–180, 1986.

[111] L.N. McCartney. Discussion: "the use of the j-integral in thermal stress crack problems,". *International Journal of Fracture*, 15(6):R217–R221, 1979.

[112] A.L. McKelvey and R.O. Ritchie. Fatigue-crack growth behavior in the superelastic and shape-memory alloy nitinol. *Metal. Mater. Trans. A*, 32(3):731–743, 2001.

[113] R.M. McMeeking and A.G. Evans. Mechanics of transformation toughening in brittle materials. *Journal of the American Ceramic Society*, 65(5):242–246, 1982.

[114] K. Mehta and A.V. Virkar. Fracture Mechanisms in Ferroelectric–Ferroelastic Lead Zirconate Titanate (Zr: Ti=0.54:0.46) Ceramics. *Journal of the American Ceramic Society*, 73(3):567–574, 1990.

[115] K.N. Melton. Deformation behavior of niti-based alloys. 1978.

[116] J.G. Merkle and H.T. Corten. J integral Analysis for the Compact Specimen, Considering Axial Force as Well as Bending Effects. Technical report, Oak Ridge National Lab., Tenn.(USA); Illinois Univ., Urbana (USA). Dept. of Theoretical and Applied Mechanics, 1973.

[117] S. Miyazaki. *Engineering Aspects of Shape Memory Alloys*. Butterworth-Heinemann, London, 1990.

[118] S. Miyazaki, K. Mizukoshi, T. Ueki, T. Sakuma, and Y. Liu. Fatigue life of ti–50 at.% ni and ti–40ni–10cu (at.%) shape memory alloy wires. *Materials Science and Engineering: A*, 273:658–663, 1999.

[119] N.B. Morgan. Medical shape memory alloy applications – the market and its products. *Mater. Sci. Eng. A*, 378:16–23, 2004.

[120] A. Needleman. A Continuum Model for Void Nucleation by Inclusion Debonding. *J. Appl. Mech.*, 54(3):525–531, 1987.

[121] J.S. Olsen, Z.L. Zhang, H. Lu, and C. Van der Eijk. Fracture of notched round-bar niti-specimens. *Engineering Fracture Mechanics*, 84:1–14, 2012.

[122] J.S. Olsen, Z.L. Zhang, H. Lu, and C. van der Eijk. Fracture of notched round-bar NiTi-specimens. *Engineering Fracture Mechanics.*, 84:1 – 14, 2012.

[123] K. Otsuka and T. Kakeshita. Science and technology of shape-memory alloys: new developments. *mrs bulletin*, 27(2):91–100, 2002.

[124] K. Otsuka and C.M. Wayman. *Shape memory materials*. Cambridge university press, 1999.

[125] K. Otsuka and C.M. Wayman, editors. *Shape Memory Materials*. Cambridge University Press, Cambridge, 1999.

[126] G. Özerim, G. Anlaş, and Z. Moumni. On crack tip stress fields in pseudoelastic shape memory alloys. *Int. J. Fract.*, 212(2):205–217, 2018.

[127] J.S.N Paine and C.A. Rogers. The response of sma hybrid composite materials to low velocity impact. *Journal of Intelligent Material Systems and Structures*, 5(4):530–535, 1994.

[128] P. Paris, H. Tada, A. Zahoor, and H. Ernst. The Theory of Instability of the Tearing Mode of Elastic-Plastic Crack Growth. In *Elastic-Plastic Fracture*, pages 5–36. ASTM International, 1979.

[129] D.M. Parks. The virtual crack extension method for nonlinear material behavior. *Computer Methods in Applied Mechanics and Engineering*, 12:353–364, 1977.

[130] A. Pineau. *Global and Local Approaches of Fracture — Transferability of Laboratory Test Results to Components*, pages 197–234. Springer New York, New York, NY, 1992.

[131] A. Pineau. Development of the local approach to fracture over the past 25 years: Theory and applications. *Int. J. Frac.*, 138(1):139–166, 2006.

[132] R.C. Pohanka, S.W. Freiman, and B.A. Bender. Effect of the Phase Transformation on the Fracture Behavior of BaTiO¡inf¿3¡/inf¿. *Journal of the American Ceramic Society*, 61(1-2):72–75, 1978.

[133] H. Prahlad and I. Chopra. Development of a strain-rate dependent model for uniaxial loading of SMA wires. *Journal of Intelligent Material Systems and Structures*, 14(14):429–442, 2003.

[134] W.D. Reinhardt and R.N. Dubey. Eulerian strain-rate as a rate of logarithmic strain. *Mech. Res. Com.*, 22(2):165–170, 1995.

[135] J. R. Rice. A Path Independent Integral and the Approximate Analysis of Strain Concentration by Notches and Cracks. *Journal of Applied Mechanics*, 35(2):379–386, 1968.

[136] J.R. Rice. Elastic-plastic models for stable crack growth. In *Mechanics and Mechanisms of Crack Growth (Proc. 1973)*, pages 14–39, 1975.

[137] J.R. Rice, R.M. McMeeking, D.M. Parks, and E.. Sorensen. Recent finite element studies in plasticity and fracture mechanics. *Computer Methods in Applied Mechanics and Engineering*, 17–18:411–442, 1979.

[138] J.R. Rice and D.M. Tracey. On the ductile enlargement of voids in triaxial stress fields. *J. Mech. Phys. Solids*, 17(3):201–217, 1969.

[139] S. Robertson and R. Ritchie. In vitro fatigue-crack growth and fracture toughness behavior of thin-walled superelastic nitinol tube for endovascular stents: A basis for defining the effect of crack-like defects. *Biomaterials*, 28:700–709, 2007.

[140] S.W. Robertson, A. Mehta, A.R. Pelton, and R.O. Ritchie. Evolution of crack-tip transformation zones in superelastic Nitinol subjected to in situ fatigue: A fracture mechanics and synchrotron X-ray microdiffraction analysis. *Acta Materialia*, 55(18):6198–6207, 2007.

[141] S.W. Robertson, A. Metha, A.R. Pelton, and R.O. Ritchie. Evolution of crack-tip transformation zones in superelastic Nitinol subjected to in situ fatigue: A fracture mechanics and synchrotron X-ray micro-diffraction analysis. *Acta Mater.*, 55:6198–6207, 2007.

[142] S.W. Robertson, A.R. Pelton, and R.O. Ritchie. Mechanical fatigue and fracture of nitinol. *International Materials Reviews*, 57(1):1–37, 2012.

[143] S.W. Robertson, A.R. Pelton, and R.O. Ritchie. Mechanical fatigue and fracture of Nitinol. *Int. Mater. Rev.*, 57(1):1–36, 2012.

[144] J. Ryhänen. Biocompatibility evolution of nickel-titanium shape memory alloy. *Academic Dissertation, Faculty of Medicine, University of Oulu, Oulu, Finland*, 1999.

[145] H. Schreier, J.J. Orteu, and M.A. Sutton. *Image Correlation for Shape, Motion and Deformation Measurements*. Springer US, 2009.

[146] B. Selvarajou, S.P. Joshi, and A. A. Benzerga. Void growth and coalescence in hexagonal close packed crystals. *J. Mech. Phys. Solids*, 125:198–224, 2019.

[147] S.A. Shabalovskaya. Biological aspects of tini alloy surfaces. *Journal de Physique IV*, 5(C8):C8–1199, 1995.

[148] J. Shaw and S. Kyriakides. Thermomechanical aspects of NiTi. *Journal of the Mechanics and Physics of Solids*, 43(8):1243–1281, 1995.

[149] C.F. Shih, B. Moran, and T. Nakamura. Energy release rate along a three-dimensional crack front in a thermally stressed body. *International Journal of Fracture*, 30:79–102, 1986.

[150] J.C. Simo and T.J.r. Hughes. *Computational Inelasticity*. Springer-Verlag, 1998.

[151] K. Siruguet and J.B. Leblond. Effect of void locking by inclusions upon the plastic behavior of porous ductile solids–I: theoretical modeling and numerical study of void growth. *Int. J Plast.*, 20(2):225–254, 2004.

[152] O.P. Sovik. *Numerical modeling of ductile fracture: A damage mechanics approach.* PhD thesis, NTNU: Norwegian University of Science and Technology, 1998.

[153] G. Stam and E. van der Giessen. Effect of reversible phase transformations on crack growth. *Mechanics of materials*, 21(1):51–71, 1995.

[154] G. Stam and E. van der Giessen. Effect of reversible phase transformations on crack growth. *Mechanics of Materials*, 21:51–71, 1995.

[155] J.K. Strelec, D.C Lagoudas, M.A. Khan, and J. Yen. Design and implementation of a shape memory alloy actuated reconfigurable airfoil. *Journal of Intelligent Material Systems and Structures*, 14(4-5):257–273, 2003.

[156] M. Tawfik, J.J. Ro, and C. Mei. Thermal post-buckling and aeroelastic behaviour of shape memory alloy reinforced plates. *Smart Materials and Structures*, 11(2):297, 2002.

[157] V. Tvergaard. On localization in ductile materials containing spherical voids. *Int. J. Fract.*, 18:237–252, 1982.

[158] V. Tvergaard. Interaction of very small voids with larger voids. *International Journal of Solids and Structures*, 35(30):3989–4000, 1998.

[159] T. Ungár, J. Frenzel, S. Gollerthan, G. Ribárik, L. Balogh, and G. Eggeler. On the competition between the stress-induced formation of martensite and dislocation plasticity during crack propagation in pseudoelastic niti shape memory alloys. *Journal of Materials Research*, 32(23):4433–4442, 2017.

[160] T. Ungár, J. Frenzel, S. Gollerthan, G. Ribárik, L. Balogh, and G. Eggeler. On the competition between the stress-induced formation of martensite and dislocation plasticity during crack propagation in pseudoelastic niti shape memory alloys. *Journal of Material Research*, pages 1–10, 2017.

[161] R. Vaidyanathan, D.C. Dunand, and U. Ramamurty. Fatigue crack-growth in shape-memory NiTi and NiTi-TiC composites. *Materials Science and Engineering, A*, 289(1–2):208–216, 2000.

[162] G.M. Vasko, P.H. Leo, and T.W. Shield. Prediction and observation of crack tip microstructure in shape memory CuAlNi single crystals. *J. Mech. Phys. Solids*, 50(9):1843–1867, 2002.

[163] F.E. Wang, W.J. Buehler, and S.J. Pickart. Crystal structure and a unique"martensitic"transition of tini. *Journal of Applied Physics*, 36(10):3232–3239, 1965.

[164] G.Z. Wang. Effect of Martensite Transformation on Fracture Behavior of Shape Memory Alloy NiTi in a Notched Specimen. *International Journal of Fracture*, 146(1):93–104, 2007.

[165] G.Z. Wang. Effect of martensite transformation on fracture behavior of shape memory alloy NiTi in a notched specimen. *Int. J. Fract.*, 146:93–104, 2007.

[166] G.Z. Wang. A finite element analysis of evolution of stress–strain and martensite transformation in front of a notch in shape memory alloy niti. *Materials Science and Engineering: A*, 460:383–391, 2007.

[167] G.Z. Wang. A finite element analysis of evolution of stress-strain and martensite transformation in front of a notch in shape memory alloy NiTi. *Mater. Sci. Engng. A*, 460–461:460–461, 2007.

[168] X.M. Wang, Y.F. Wang, A. Baruj, G. Eggeler, and Z.F. Yue. On the Formation of Martensite in Front of Cracks in Pseudoelastic Shape Memory Alloys. *Materials Science and Engineering: A*, 394(1):393–398, 2005.

[169] C.E. Willey, B. Huettl, and S.W. Hill. Design and development of a miniature mechanisms tool-kit for micro spacecraft. In *35 th Aerospace Mechanisms Symposium*, volume 1, 2001.

[170] M.H. Wu and L.M. Schetky. Industrial applications for shape memory alloys. In *Proceedings of the international conference on shape memory and superelastic technologies, Pacific Grove, California*, volume 44, 2000.

[171] H. Xiao, O.T. Bruhns, and A. Meyers. Logarithmic strain, logarithmic spin and logarithmic rate. *Acta Mech.*, 124(1-4):89–105, 1997.

[172] L. Xu, T. Baxevanis, and D.C. Lagoudas. A three-dimensional constitutive

model for the martensitic transformation in polycrystalline shape memory alloys under large deformation. *Smart Mater. Struct.*, 28(7):074004, 2019.

[173] W. Yan and Y.W. Mai. Theoretical consideration on the fracture of shape memory alloys. In *IUTAM Symposium on Mechanics and Reliability of Actuating Materials*, pages 217–226. Springer, 2006.

[174] W. Yan, C.H. Wang, X.P. Zhang, and Y.W. Mai. Effect of transformation volume contraction on the toughness of superelastic shape memory alloys. *Smart Mater. Struct.*, 11:947–955, 2002.

[175] S. Yi and S. Gao. Fracture toughening mechanism of shape memory alloys due to martensite transformation. *International journal of solids and structures*, 37(38):5315–5327, 2000.

[176] S. Yi and S. Gao. Fracture toughening mechanism of shape memory alloys due to martensite transformation. *Int. J. Solids Struct.*, 37:5315–5327, 2000.

[177] S. Yi, S. Gao, and L. Shen. Fracture toughening mechanism of shape memory alloys under mixed-mode loading due to martensite transformation. *International Journal of Solids and Structures*, 38(24-25):4463–4476, 2001.

[178] S. Yi, S. Gao, and S. Shen. Fracture toughening mechanism of shape memory alloys under mixed-mode loading due to martensite transformation. *Int. J. Solids Struct.*, 38:4463–4476, 2001.

[179] M.H. Yoo and C.L. Fu. Cleavage fracture of ordered intermetallic alloys. In *High Temperature Aluminides and Intermetallics*, pages 470–478. Elsevier, 1992.

[180] Y. You, X. Gu, Y. Zhang, Z. Moumni, G. Anlaş, and W. Zhang. Effect of thermomechanical coupling on stress-induced martensitic transformation around

the crack tip of edge cracked shape memory alloy. *Int. J. of Fract.*, 216(1):123–133, 2019.

[181] M. Zhang and T. Baxevanis. An Extended 3D Finite Strain Constitutive Model for Shape Memory Alloys. 2020. submitted.

[182] X. Zhu. Review: J-integral resistance curve testing and evaluation. *Journal of Zhejiang University SCIENCE A*, 10(11):1541–1560, 2009.

[183] X. Zhu and J. Joyce. Review of fracture toughness (G, K, J, CTOD, CTOA) testing and standardization. *Engineering Fracture Mechanics*, 85:1–46, 2012.

7 Appendix

7.1 Numerical implementation for η-elastic implementations.

7.1.1 η^{el} and γ^{el}-factors for disk-shaped CT specimen.

ASTM standards allow for fracture toughness measurement from disk-shaped CT specimen, for which η^{el} and γ^{el} read as

$$\eta^{el}_{DCT} = 1.55 + 2.19\left(\frac{b}{W}\right), \tag{40}$$

$$\gamma^{el}_{DCT} = 0.55 + 3.12\left(\frac{b}{W}\right). \tag{41}$$

Both η^{el} and γ^{el} have been calculated using contour integral approach in FEM software ABAQUS for different crack sized geometry.

7.1.2 Further details on the numerical comparison between the proposed method and ASTM standards

Further details on the investigation of the error in the J_{I_C}-measurement introduced by the proposed methodology and [4] are given here. Since the difference between the two methodologies is limited to the calculation of J^{el}, the constitutive model adopted in the finite element analysis only accommodates the change in the elastic properties in the absence of transformation or orientation strains.

7.1.3 Constitutive model

The Marlow hyperelastic model, implemented in the commercial software Abaqus, is used to capture the isothermal change in the elastic properties in the absence of transformation or orientation strains.

The isothermal version of the model is based on a strain energy density potential of the form

$$U = U_{dev}\left(\bar{I}_1\right) + U_{vol}\left(J\right), \tag{42}$$

where U is the strain energy per unit reference volume, U_{dev} and U_{vol} are the deviatoric and volumetric parts of U, respectively, $\bar{I}_1$ is the first deviatoric strain invariant defined as

$$\bar{I}_1 = \bar{\lambda}_1^2 + \bar{\lambda}_2^2 + \bar{\lambda}_3^2, \tag{43}$$

$\bar{\lambda}_i = J^{-\frac{1}{3}}\lambda_i$ are the deviatoric streches, J is the total volume ratio, and λ_i are the principal stretches.

The deviatoric part of U is defined by uniaxial data provided by an SMA model [87] excluding the transformation strains, allowing only for the the change in the elastic properties (see Fig. 3 in the paper) while the volumetric part is defined through the Poisson's ratio, which is set to 0.3.

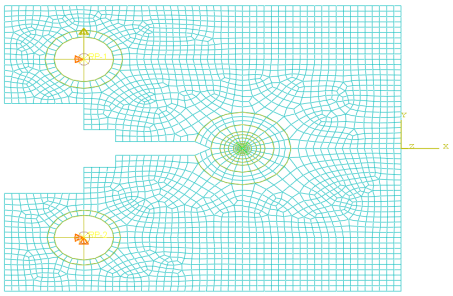

Figure 36: Finite element mesh of the CT geometry used in the numerical simulations.

7.1.4 Problem description

The finite element analysis is performed on a CT geometry under plane strain loading. A finite element mesh of 2849 plane strain, eight-noded, isoparametric quadrilateral elements is designed for the analysis (Fig 36). Singular crack tip elements are used for the J-integral evaluation, shaped as isosceles triangles focused into the crack tip and placed in angular intervals of $\pi/24$. These elements are created by collapsing one side of the eight-noded quadrilaterals and assigning each of the crack tip nodes common degrees of freedom, with the midside nodes on the sides connected to the crack tip moved on the 1/4 points nearest the crack tip. The interpolation function for such elements exhibits a singularity of the form $Br^{-1/2}$ in displacement derivatives (Fig. 37).

Displacement/rotation boundary conditions are applied at reference nodes placed at the center of both pinholes to simulate CT experiments. The nodes on each pinhole surface are kinematically constrained to the corresponding reference nodes so that their translational/rotational degrees of freedom coincide with those of the reference nodes. One of the reference nodes is displaced in the direction perpendicular to the crack line (y-direction) while the other reference node is fixed but allowed to rotate.

The J-value is calculated from the load–load line displacement record using the

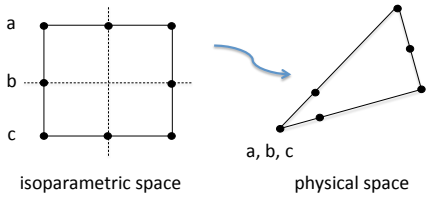

Figure 37: Singularity elements used. One side of the eight-noded element is collapsed so that all three nodes – a, b and c – are placed on the same geometric location (at the crack tip). The midside nodes on the sides connected to the crack tip are moved on the 1/4 points nearest the crack tip.

proposed methodology and the ASTM standards, and through the domain integral method, described in [129, 95, 149],

$$J_A = -\int_A \left[W \frac{\partial q}{\partial x_1} - \sigma_{ji} \frac{\partial q}{\partial x_j} \frac{\partial u_i}{\partial x_1} \right] dA, \tag{44}$$

where A is the region enclosed by an outer circular contour, the first ring of elements directly connected to the crack tip and the crack faces, and q is a function that is equal to unity at the inner boundary of A and equal to zero at the outer boundary.